









The Role of Cloud Radiative Effects in the Propagating Southern Annular Mode

Jian Lu¹ , Bryce E. Harrop¹ , Sandro W. Lubis¹ , Samuel Smith^{2,3} , Gang Chen⁴ , and L. Ruby Leung¹ 

¹Pacific Northwest National Laboratory, Richland, WA, USA, ²Indiana University, Bloomington, IN, USA, ³University of Chicago, Chicago, IL, USA, ⁴University of California, Los Angeles, Los Angeles, CA, USA

Key Points:

- Cloud locking technique is used to isolate the interactive cloud radiative effect (CRE) on the Southern Annular Mode (SAM)
- Cloud radiative effect boosts the persistence of SAM as the leading EOF of the Southern Hemisphere zonal wind
- The interactive CRE feedback acts to weaken the cross-EOF interaction and counter the poleward propagation of the zonal wind

Correspondence to:

J. Lu,
jian.lu@pnnl.gov

Citation:

Lu, J., Harrop, B. E., Lubis, S. W., Smith, S., Chen, G., & Leung, L. R. (2024). The role of cloud radiative effects in the propagating Southern Annular Mode. *Journal of Geophysical Research: Atmospheres*, 129, e2023JD040428. <https://doi.org/10.1029/2023JD040428>

Received 2 DEC 2023
 Accepted 2 APR 2024

Abstract The Southern Annular Mode (SAM) is the most dominant natural mode of variability in the mid-latitudes of the Southern Hemisphere (SH). However, both the sign and magnitude of the feedbacks from the diabatic processes, especially those associated with clouds, onto the SAM remain elusive. By applying the cloud locking technique to the Energy Exascale Earth System Model (E3SM) atmosphere model, this study isolates the positive feedback from the cloud radiative effect (CRE) to the SAM. Feedback analysis based on a wave activity-zonal momentum interaction framework corroborates this weak but positive feedback. While the magnitude of the CRE feedback appears to be secondary compared to the feedbacks from the dry and other diabatic processes, the indirect CRE effects through the interaction with other dynamical and thermodynamical processes appear to play as important a role as the direct CRE in the life cycle of the SAM. The cross-EOF analysis further reveals the obstructive effect of the interactive CRE on the propagation mode of the SH zonal wind directly through the CRE wave source and/or indirectly through modulating other diabatic processes. As a result, the propagation mode becomes more persistent and the SAM it represents becomes more predictable when the interactive CRE is disabled by cloud locking. Future efforts on inter-model comparisons of CRE-denial experiments are important to build consensus on the dynamical feedback of CRE.

Plain Language Summary The annular mode is the most dominant mode of variability in the mid-latitude atmospheric circulation system. Its origin, maintenance, and feedback mechanisms have long been the focus of atmospheric dynamics research. While its dry mechanisms are well understood, the role of the diabatic processes in the midlatitude storm tracks, especially the radiative effects of the cloud fields that evolve together with the storms, have not been quantified. Even the sign of the diabatic feedback to the annular mode remains a topic of debate. By disabling the cloud radiative feedback through a cloud-locking technique that decorrelates the cloud fields with other dry and moist components in an atmospheric model, we are able to isolate the cloud radiative effect (CRE) throughout the life cycle of the Southern Annular Mode (SAM). Compared to the case with interactive CRE, the propagating SAM becomes more persistent and predictable in the cloud-locking run, although the overall diabatic feedback to the standing dipole representation of the SAM is somewhat attenuated in this run. The diabatic and CRE feedbacks to the SAM identified here epitomize the sensitivity of the leading mode of the atmospheric variability to the model representation of the diabatic processes.

1. Introduction

The Southern Annular Mode (SAM) is one of the most extensively studied modes of variability on subseasonal time scales in the climate system (Thompson & Wallace, 2000). In a first-order picture, an annular mode is a barotropic phenomenon with its initiation attributable to random bursts of eddy momentum convergence/divergence, often resulting from wave breaking (Benedict et al., 2004; Feldstein & Lee, 1996; Franzke et al., 2003), and its dipole structure attributable to the conservation of zonal momentum and mass by fluid motions (Gerber & Vallis, 2005). Annular modes owe their longer-than-synoptic-scale persistence to the positive feedbacks via both barotropic (Burrows et al., 2017; Lorenz, 2014; Lorenz & Hartmann, 2001; Nie et al., 2014) and baroclinic processes (e.g., Hassanzadeh & Kuang, 2019; Robinson, 2000). The barotropic feedback arises from the organization of the upper-level wave propagation by the anomalous zonal wind in such a way that the wave activity propagates away from (into) the positive (negative) zonal wind anomalies, resulting in an eddy momentum forcing dipole that reinforces the original zonal wind anomalies. The Rossby wave chromatography analysis of Lorenz (2014) found that both wave dissipation at the critical level and wave reflection can provide positive feedback mechanisms for the enhancement of the zonal wind on the poleward side of the mean jet

© 2024 The Authors.
 This is an open access article under the terms of the [Creative Commons Attribution-NonCommercial License](https://creativecommons.org/licenses/by/4.0/), which permits use, distribution and reproduction in any medium, provided the original work is properly cited and is not used for commercial purposes.

(Lorenz, 2023). In response to the initial eddy momentum forcing, a pair of enhanced and reduced baroclinicity anomalies emerges in the adjustment to the interior torque via the surface friction. These baroclinicity changes then generate more vertical wave activity fluxes to feed into the horizontal propagation that contributes to the positive feedback (Robinson, 2000). A methodical feedback framework constructed using the overriding technique has shown that the annular mode is the optimal feedback mode between the synoptic eddies and the zonal advection effect of the zonal wind anomalies, laying a theoretical foundation for the dry dynamics of the annular mode (Chen et al., 2020).

While the dry dynamics of the annular mode are well understood, the dynamics community is only beginning to appreciate the role of diabatic feedbacks in the leading modes of atmospheric variability. For the case of the annular modes, even the sign of the diabatic feedbacks to the annular mode persistence remains an issue of debate. Some (e.g., Xia & Chang, 2014; Lei Wang, personal communications) found that the diabatic heating due to latent heating exerts a damping effect on the annular mode by reducing the lower-level baroclinicity, making it much shorter lived. Others have suggested a positive role of the diabatic heating in prolonging the memory of the annular mode (Lutsko & Hell, 2021; Papavasileiou et al., 2020; Woollings et al., 2016). Understanding and quantifying the diabatic feedbacks are important, as they might underly the equatorward bias in the mean westerly jet position in the state-of-the-art climate models, which has been shown to be related to the over-persistence of the SAM and the overestimation of the jet shift response to climate change forcings (Bracegirdle et al., 2020; Gerber et al., 2008).

Among the diabatic processes, the cloud radiative effect (CRE) is perhaps the largest source of uncertainty in climate sensitivity, a concept of how much the global mean surface temperature warms in response to the forcing of doubling the CO₂ concentration. In addition, CRE has been found an important role in the poleward shift of the westerly jet under the forcing of increasing greenhouse gases (e.g., Li et al., 2019; Voigt et al., 2020; Voigt & Shaw, 2016). To the authors' knowledge, the role of CRE in shaping the spatiotemporal characteristics of SAM has not been previously investigated, although highly organized structures have been found in the cloud incidence and the associated CRE along with the SAM (Li & Thompson, 2016; Liu et al., 2020; Wall et al., 2022).

It is the central goal of this study to isolate the CRE feedback to the SAM and its propagation through a cloud locking technique in a full AGCM. The CRE feedback identified as such includes not only the “direct” heating effect through the radiatively active cloud properties, but also the “indirect” interactions of cloud with other thermodynamic and dynamic variables due to their co-variations in the atmosphere, hence referred to as the “interactive” CRE feedback in the context of this study. This interactive CRE must be distinguished from the feedback diagnosed from the observations or full model simulations (e.g., Papavasileiou et al., 2020; Woollings et al., 2016), which captures mainly the “direct” feedback. The interactive CRE feedback should also be distinguished from the CRE feedback of the complete CRE denial experiments, such as those conducted in the COOKIE project (Clouds On/Off Klimate Intercomparison Experiment Project, Stevens et al., 2012), in which both the interactive and the mean CRE heating in the atmosphere are eliminated, the intervention being so drastic that the mean climate shifts to a substantially different state (see Harrop et al., 2024). It is difficult to use the COOKIE-style experiments to evaluate the feedback of CRE because the mean state changes so much that the small perturbation assumption for linear feedback analysis is violated, while the COOKIE-style experiments may still be useful for studying the CRE in the mean climate. The different analysis and modeling approaches may be the reason behind the confusions regarding the diabatic feedbacks in the annular mode literature. In this study, we quantify the “direct” CRE feedback to the SAM using a finite-amplitude wave activity (FAWA) budget analysis, which can trace the horizontal convergence/divergence of eddy momentum/wave activity to barotropic, baroclinic, and diabatic sources. As to be shown in this study, the interactive CRE isolated via cloud locking contains more than the “direct” CRE; it is the total interactive CRE that gives rise to detectable changes in the characteristics of the SAM.

On the other hand, growing evidence indicates that the leading mode of the mid-latitude westerly jet variability in both hemispheres should be interpreted as a propagation mode (Sheshadri & Plumb, 2017; Lubis & Hassanzadeh, 2021, LH21 hereafter; Lubis & Hassanzadeh, 2023; Smith et al., 2024) and better represented by a principal oscillation pattern (POP, von Storch et al., 1988; Penland, 1989). Therefore, in addition to the conventional single EOF-based feedback analysis, we also perform a Dynamical Mode Decomposition (DMD, Schmid & Sesterhenn, 2008; Bai et al., 2017) analysis based on the first two EOFs of the SH zonal wind to identify the leading POP and to quantify the cross-EOF interactions. Both single-EOF and cross-EOF perspectives will be provided in

this study, the former to connect with the large majority of literature on the annular mode (which is conventionally defined based on a single EOF), and the latter to provide a more up-to-date view of the annular mode of mid-latitude variability. In the end, we attempt to reconcile the two views to provide a more comprehensive understanding of the dynamical feedback of the CRE.

In what follows, we first describe the model experiments and analysis methods used in the current study in Section 2. The results will be described in Section 3, which includes the discussion of the effects of the CRE on the characteristics and feedbacks of the SAM from both a single-EOF and a cross-EOF perspective. The paper will conclude with a summary and discussion.

2. Model Experiments and Analysis Methods

2.1. Control and Cloud Locking Experiments With E3SM

The AGCM for the experiments of this study is the atmospheric component of the Energy Exascale Earth System Model v1 (Golaz et al., 2019), which will be referred to as E3SM hereafter. All experiments are run as “AMIP” style with realistic land-sea geography, an active land model, and prescribed annually repeating sea surface temperatures (SSTs) and sea-ice concentrations. The control run (CTRL) uses the SSTs, sea-ice concentrations, and atmospheric forcings representative of the present-day climate conditions (a 10-year average centered on year 2000). CTRL is integrated for 20 years after a 30-year spin-up, which is to ensure the global soil moisture is in equilibrium prior to running production simulations.

The cloud-locking experiment (CL hereafter) makes use of the approach of Middlemas et al. (2019) to isolate the interactive CRE. This is achieved by prescribing the cloud optical properties from the CTRL simulation in the CL simulation at the frequency of radiative transfer calls made by the AGCM. As such, 10 cloud variables at hourly frequency must be written out and stored for the cloud locking purpose during the production of CTRL. Similar cloud-locking experiments were also performed by Grise et al. (2019) to quantify the impact of CRE in the extratropical cyclones. The cloud-locking experiment is fundamentally different from the complete CRE denial experiments, such as those conducted in the COOKIE project (Stevens et al., 2012), in that cloud-locking does not eliminate the mean CRE heating in the atmosphere, but only decouples the CRE from the dynamics and other physical processes, removing any covariance between them on high frequency time scales relevant to the evolution of storm systems within the SAM. The CL run is also 20 years long.

Disabling the interactive CRE using cloud-locking in E3SM can lead to systematic drift in the climate state. Figure 1 shows the annual mean, zonal mean difference in CRE and the circulation metrics due to cloud-locking. The total time and zonal mean CRE difference is dominated by longwave (LW) radiation (Figure 1b), featuring a positive heating in the upper troposphere and a cooling in the lower stratosphere, which, owing to the poleward sloping tropopause, can give rise to an enhanced differential heating between the tropics and the extratropics. The magnitudes of the CRE changes are modest (with peak values less than 0.5 K day^{-1}). However, since the differential heating near the extratropical tropopause is most efficient in driving the poleward shift of the eddy-driven jet (Chen et al., 2020; Hassanzadeh & Kuang, 2016a), it may contribute to driving the poleward shift in the zonal mean zonal wind (by $\sim 1.2^\circ$ latitude), eddy kinetic energy, and finite-amplitude wave activity. The poleward shifts in the dynamic structures may confound the detection of the CRE feedback in the SAM—something to keep in mind in the interpretation of the diagnostic result of the direct CRE feedback later in this study. Interestingly, the greenhouse gas-forced cloud response also shares similar CRE structure in the upper-troposphere and lower-stratosphere, which has been found to contribute to at least half of the total shift of the zonal mean zonal wind under the forcing of increasing greenhouse gases (Ceppi & Hartman, 2016; Voigt & Shaw, 2016).

2.2. FAWA Budget With Diabatic Wave Source

For the SAM feedback analysis, we adopt the zonal momentum-FAWA ($\bar{u} \sim A$) interaction framework of Nie et al. (2014, also Chen et al., 2013; Burrows et al., 2017). This framework leverages the non-acceleration relation (in the conservative limit) that the upward wave activity flux tends to be largely converted to horizontal wave activity flux to accelerate/decelerate the zonal mean momentum at the core of the eddy-driven jet (e.g., Vallis, 2007). For the general, non-conservative case, the portion of conversion rate can be significantly less than unity due to the non-negligible dissipation or non-conservative processes (Lorenz, 2022), while the partitioning to

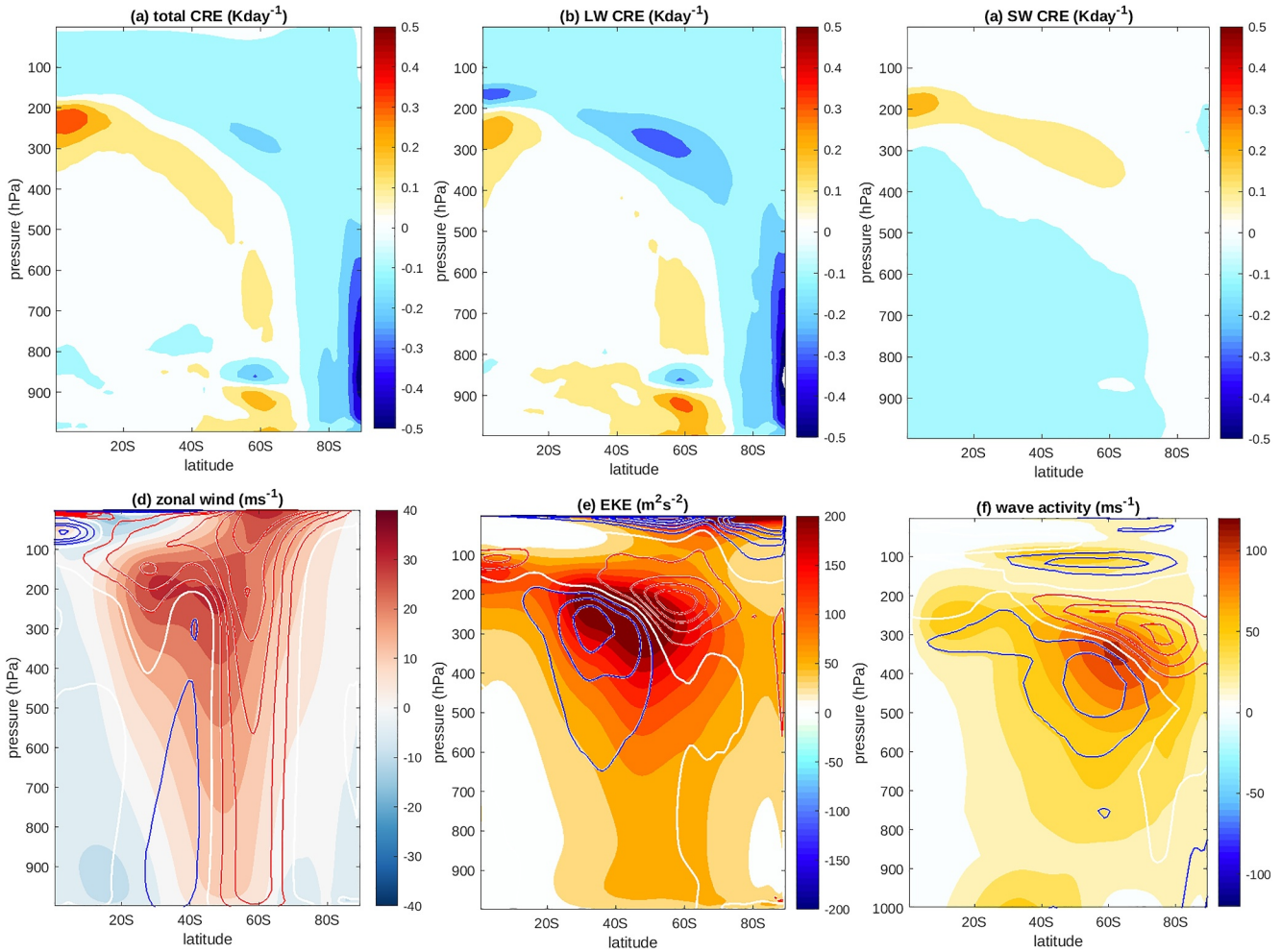


Figure 1. Changes in the CRE heating rates and the zonal mean circulation metrics due to cloud-locking. Note that in the lower panels, the contours are for the change between the CL run and the CTRL run, and the shading indicates the climatological mean fields from CTRL. The contour intervals in (d)–(f) are 2.5 ms^{-1} , $4 \text{ m}^2 \text{ s}^{-2}$, 3 ms^{-1} , respectively.

the horizontal flux can be further modulated by the presence of diabatic wave sources. Nevertheless, the generalized Eliassen-Palm relationship (e.g., Lubis et al., 2018; Nakamura & Solomon, 2010) allows the substitution of the eddy momentum flux convergence (EMFC) in terms of the baroclinic, diabatic, and dissipative wave sources.

Following Nie et al. (2014), the $\bar{u} \sim A$ interaction system in pressure pseudoheight coordinate ($z = -H \ln\left(\frac{p}{p_0}\right)$, where H is scale height and set to be 7 km) is formulated as

$$\frac{\partial \langle \bar{u} \rangle}{\partial t} \approx -\frac{1}{\cos^2 \phi} \frac{\partial}{\partial \phi} \left(\langle \bar{u}'v' \rangle \cos^2 \phi \right) + \langle F_r \rangle \quad (1a)$$

$$\frac{\partial \langle A \rangle_{up}}{\partial t} = \frac{1}{\cos^2 \phi} \frac{\partial}{\partial \phi} \left(\langle \bar{u}'v' \rangle_{up} \cos^2 \phi \right) - \frac{f}{H_z} \left\langle \frac{\partial}{\partial z} \left(e^{-z/H} v' \theta' \right) \right\rangle_{up} - \frac{f e^{\tilde{\pi}}}{\cos \phi} \left\langle \frac{\partial}{\partial z} \left(\frac{\tilde{Q} e^{(\kappa-1)z/H}}{c_p \partial \tilde{\theta} / \partial z} \right) \right\rangle_{up} - \langle D \rangle. \quad (1b)$$

See Nakamura and Zhu (2010) for the exact derivation of 1b. The notation in 1b follows those of Huang and Nakamura (2017). The second rhs term is the baroclinic contribution (B) to the wave activity growth, which

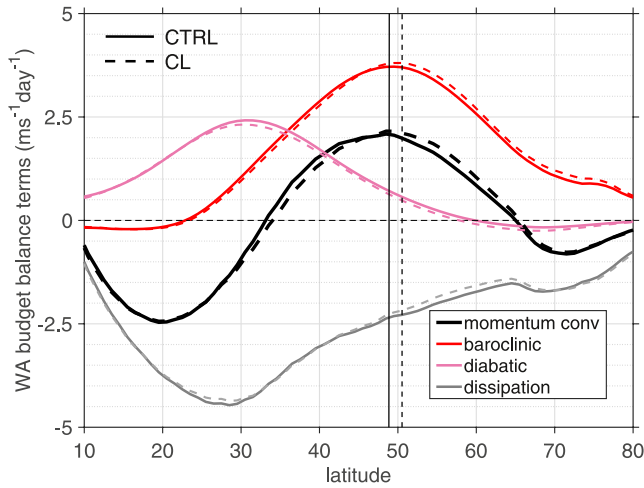


Figure 2. The climatological mean FAWA budget in the Southern Hemisphere. Solid curves (dashed curves) are for the CTRL (CL) simulation. The vertical line denotes the location of the near surface westerly jet. The annual mean jet in CL shifts poleward about 1.2° latitude due to cloud locking.

troposphere, and it is through the change in the upper-tropospheric eddy momentum flux that any eddy feedback to the zonal wind can be realized. Choosing a 5 km cutoff for the troposphere is equivalent to truncating the tropospheric dynamics to a two-layer conceptual model, where only the barotropic and first baroclinic vertical modes are considered. Moreover, the quasi-geostrophic diagnostics is more applicable for the mid-to-upper troposphere, because quasi-geostrophy is no longer valid in the planetary boundary layer, where the near surface isentropes often intersect with the surface (Schneider, 2005).

The climatological balance among the right-hand-side terms of 1b for both CTRL (solid lines) and CL (dashed lines) simulations is presented in Figure 2. One can see that the diabatic wave source (\mathcal{H}) plays an important part in the four-way balance in the upper-tropospheric wave activity budget. The negativity of the \mathcal{D} term in climatology is consistent with its dissipative effect on the positive definite wave activity. This budget provides a simple two-mode view of the maintenance of the midlatitude eddy-driven jet: Both the diabatic (\mathcal{H}) and the baroclinic (\mathcal{B}) terms are important suppliers of wave activity to the upper troposphere (see the red and pink lines in Figure 2), where much of the wave activity gets dissipated by wave breaking, with the remainder propagating away meridionally. By definition, the meridional wave flux is a negative eddy momentum flux; it is the eddy momentum divergence/convergence associated with this wave activity propagation that transports eddy momentum poleward to sustain the eddy-driven westerly wind in the midlatitude troposphere. We also note that cloud locking does not bring about any qualitative change in the basic wave activity balance compared to CTRL.

Since the EMFC is dominated by upper-troposphere and highly correlated with the column-averaged EMFC (Nie et al., 2014; Smith et al., 2024), we can substitute 1b into 1a through the EMFC term to obtain

$$\frac{\partial \langle \bar{u} \rangle}{\partial t} \approx - \underbrace{\gamma \frac{\partial \langle A \rangle_{up}}{\partial t}}_A - \underbrace{\gamma \frac{f}{H_z} \left\langle \frac{\partial}{\partial z} \left(e^{-z/H} \overline{v' \theta'} \right) \right\rangle_{up}}_B - \underbrace{\gamma \frac{f e^{\tilde{z}}}{\cos \phi} \left\langle \frac{\partial}{\partial z} \left(\frac{\dot{Q} e^{(\kappa-1)z/H}}{c_p \partial \tilde{\theta} / \partial z} \right) \right\rangle_{up}}_H - \underbrace{\gamma \langle D \rangle}_D - \frac{1}{\tau_f} \langle \bar{u} \rangle \quad (3)$$

where $\gamma = \frac{4}{9}$ is a rescaling factor arising from the ratio of the column-averaged EMFC versus the upper-tropospherically averaged EMFC (Lorenz, 2023; Smith et al., 2024); the column friction term in 1a has been parameterized in a linear form with a damping time scale of τ_f following Chen and Plumb (2009).

2.3. Quantifying the SAM Feedbacks

In order to quantify the feedbacks to the SAM (or zonal index) from the processes expressed in 3, following Lorenz and Hartmann (2001), we project Equation 3 onto the leading EOF pattern of the barotropic zonal wind to derive the governing equation for the evolution of the zonal index z :

corresponds to the vertical Eliassen-Palm flux from the mid-troposphere; the third term on the rhs for the diabatic wave source (\mathcal{H}) is explicitly computed (as in Wang et al., 2021), as eddy diabatic processes are the focus of the current investigation; the last term on the rhs denotes the dissipation of FAWA due to wave breaking (\mathcal{D}), which is calculated as the residual of the FAWA budget equation. All the eddy terms are computed using 6 hourly data, as sub-daily eddy variations can contribute significantly to the eddy fluxes (Ma et al., 2017). $\langle \cdot \rangle$ represents the geometric transform that defines FAWA for the “eddy” component of the field in the question (e.g., Nakamura & Solomon, 2010). The angle brackets denote a density-weighted vertical average, with the subscript up for the average between 5 and 16 km:

$$\langle \langle \cdot \rangle \rangle_{up} \equiv \frac{\int_5^{16} e^{-z/H} \langle \cdot \rangle dz}{H_z} \quad (2)$$

where H_z is the density-weighted pseudoheight between 5 and 16 km.

The reason for choosing the upper-tropospheric average is two-fold: setting the cutoff level at 5 km targets the effect of the diabatic wave sources, which tend to be accentuated in the mid-troposphere in the mid-latitudes; the eddy momentum forcing for the zonal wind is concentrated in the upper-

$$\frac{\partial z}{\partial t} = m_A + m_B + m_H + m_D - \frac{1}{\tau_f} z \quad (4)$$

Similar to Lorenz and Hartmann (2001), we further parameterize the m terms on the rhs in a linear form of z :

$$\frac{\partial z}{\partial t} = b_A z + b_B z + b_H z + b_D z - \frac{1}{\tau_f} z \quad (5)$$

where b_A , b_B , b_H , and b_D denote the eddy feedbacks due to wave activity tendency, baroclinic processes, diabatic processes, and FAWA dissipation processes, respectively. These feedback parameters can be estimated using lagged regression, as described in Simpson et al. (2013). Specifically, we first regress the time series of the zonal index z and the total upper-tropospheric EMFC (i.e., $m_{uv} = m_A + m_B + m_H + m_D$) against the normalized z at lag l (positive l means z leading m), with their regression coefficients denoted as $\beta_z(l)$ and $\beta_m(l)$, respectively. This is then followed by the regressions for all the components of m . This method of estimating feedbacks is based on the understanding that feedbacks only operate after the initial zonal index response to an impulse forcing fades away, which often takes about a week. This is supported by idealized modeling studies (e.g., Chen & Plumb, 2009), which showed that the autocorrelation of the EMFC is characterized by a damped oscillator over several days and its persistence over a week should be attributed to the modulation of the zonal wind. Therefore, the following relationship is assumed to hold after a week or so:

$$\beta_m(l) z = b \beta_z(l) z,$$

where the lhs is the parameterized m at lag l and the rhs the signal in z at lag l that feedbacks to the eddies. The corresponding EMFC feedback parameter can then be computed as $b = \frac{\beta_m(l)}{\beta_z(l)}$. In a similar way, the feedback parameter for each of the feedback processes described in 5 can also be estimated. For example, the diabatic feedback is computed as $b_D = \frac{\beta_{m_D}(l)}{\beta_z(l)}$. In addition, since we have 6-hourly output for all the diabatic terms, including condensational heating, longwave clearsky heating, shortwave clearsky heating, longwave cloud heating, and shortwave cloud heating, we can further decompose the diabatic feedback into the constituent diabatic processes. The uncertainty in the feedback parameters is quantified using the bootstrapping method as explained in Simpson et al. (2013, their Appendix).

Finally, similar projections and feedback analysis can be performed for the second EOF. These projection time series for both EOF1 and EOF2 (denoted by z_1 and z_2 , respectively) are used later in the cross-EOF momentum budget analysis. Positive z_1 indicates a dipolar wind pattern with a positive anomaly poleward and a negative anomaly equatorward of the mean jet; positive z_2 indicates a narrowing and strengthening of the westerly jet. To quantify the propagation characteristics of the zonal wind variability, we also feed the time series of z_1 and z_2 into the Dynamic Mode Decomposition (DMD) algorithm (Bai et al., 2017) to learn the matrix operator \mathbf{K} that maps the time series from time t to time $t + \tau$ and to extract the leading DMD mode:

$$\begin{bmatrix} z_1(t + \tau) \\ z_2(t + \tau) \end{bmatrix} = \mathbf{K} \begin{bmatrix} z_1(t) \\ z_2(t) \end{bmatrix} = \begin{bmatrix} k_{11} & k_{12} \\ k_{21} & k_{22} \end{bmatrix} \begin{bmatrix} z_1(t) \\ z_2(t) \end{bmatrix} \quad (6)$$

Lubis and Hassanzadeh (2023) performed similar DMD analysis on several reanalysis data and data simulated by the latest climate models. It is straightforward to show that the corresponding continuous system of 6 has complex eigenvalues, corresponding to a propagating DMD mode, if the entries in the matrix \mathbf{K} satisfy the criterion:

$$(k_{11} - k_{22})^2 + 4k_{12}k_{21} < 0, \quad (7)$$

which turns out to be in the same form as the necessary and sufficient condition for propagation introduced in Lubis and Hassanzadeh (2021). This quantity will be referred to as the Lubis-Hassanzadeh Criterion (LHC) and will be used to indicate whether the SAM simulated in the CTRL and CL experiments is in the propagation regime. However, we must note that the LHC, when satisfying (7), is related to the period of the propagation as follows:

$$LHC = -4e^{-2\sigma T} \sin^2(2\pi T^{-1}\tau) \quad (8)$$

where σ and T are the decay rate and period of the propagation DMD mode. Thus, a larger LHC does not necessarily correspond to a shorter propagation period T , because the decay rate may also change. See the Appendix for the derivation of 8.

It has been understood that the dynamics governing the midlatitude zonal momentum are non-normal (Hassanzadeh & Kuang, 2016b; Ioannou, 1995; Navarra, 1993), and the matrix \mathbf{K} for zonal index evolution is generally nondiagonal. Once the matrix \mathbf{K} is learned from the time series of the z_1 and z_2 , the eigenmode decomposition of the matrix \mathbf{K} gives

$$\mathbf{K} = \mathbf{V} \exp(\mathbf{\Lambda} \tau) \mathbf{V}^{-1},$$

where \mathbf{V} is the eigenvector matrix and $\mathbf{\Lambda}$ is a diagonal matrix containing the eigenvalues of \mathbf{K} . The eigenvectors in \mathbf{V} indicate the spatial information of the DMD modes, and eigenvalues the temporal information of the DMD modes. For a stable dynamical system, the diagonals of $\mathbf{\Lambda}$ all have a negative real part, indicating that the z_1 , z_2 anomalies decay with time in the eigenvector space (Penland, 1989). Unlike EOFs, the DMD modes are sorted by the eigenvalues in $\mathbf{\Lambda}$, and thus not necessarily orthogonal to each other (i.e., \mathbf{V}^{-1} differs from \mathbf{V}^T), anomalies governed by nonnormal dynamics can grow through nonnormal interference (Farrell & Ioannou, 1996). Since only two EOFs are considered here (to facilitate a comparison with LH21), the DMD analysis can result in either two real eigenvalues for damped modes, or a pair of complex conjugates, indicating a propagation mode.

3. Results

3.1. Single EOF Diagnostic Framework

First, we compare the autocorrelation of the SAM index between the CTRL and CL experiments. The e-folding time of SAM in the control run is 10.44 ± 0.81 days, which is only marginally larger than the SAM e-folding time in the CL run (8.9 ± 0.65 days). The 95% confidence intervals for the e-folding time are estimated using the procedure of Gerber et al. (2008), which assumes that the SAM index can be modeled as a first order autoregressive process (AR1). We also estimate the uncertainties in the autocorrelation and the decorrelation time and represent them in terms of one standard deviations as whiskers and shading in Figure 3, respectively. The overlaps of the uncertainty ranges between the control and CL runs suggest that the change in the SAM e-folding time due to disabling the interactive CRE is only marginally significant at best. However, if we divide the total length of the data into four 5-year chunks and recalculate the e-folding time for both the CTRL and CL cases, we find only four out of a total of 16 comparisons that give a longer e-folding time for CL than CTRL. This suggests a coin-flip probability (for 16 flips) of 97.2% for the SAM to be more persistent in CTRL than CL:

$$P(4 \text{ choose } 16) = \text{factorial}(16)/\text{factorial}(4)/\text{factorial}(12)/2^{16} = 2.8\%$$

Thus, some confidence can be placed in the constructive effect of the interactive CRE on the SAM persistence.

The positive CRE effect on the SAM persistence is corroborated by the SAM feedback budget analysis as shown in Figure 4. Positive feedback to the annual mode is often characterized by the positive correlation when the zonal index leads the feedback terms at time scale longer than the eddy lifetime (Lorenz & Hartmann, 2001). This characteristic is also present in the lagged regression between the EMFC and the SAM index in both the CTRL and CL runs (Figures 4a and 4c, the regressions are shown in for the benefit of linear additivity). The EMFC feedback (coefficient b in Figures 4b and 4d) is slightly larger in CTRL than CL, providing the stronger feedback to maintain the longer persistence of the zonal index in the former.

Surprisingly, the diabatic term contributes as much as the baroclinic term to the positive EMFC feedback between lag 8 and lag 16 (red lines in Figures 4b and 4d), suggesting the first-order importance of the diabatic processes in shaping the time scale of the SAM. The major negative feedback comes from the dissipation of wave activity (Figure 4b, gray line). This is in contrast with a similar feedback analysis by Nie et al. (2014), who found positive feedback from dissipation. This is mainly because they neglected the diabatic wave source (the third term in Equation 3) when estimating the dissipation effect as a residual, and consequently the contribution from the

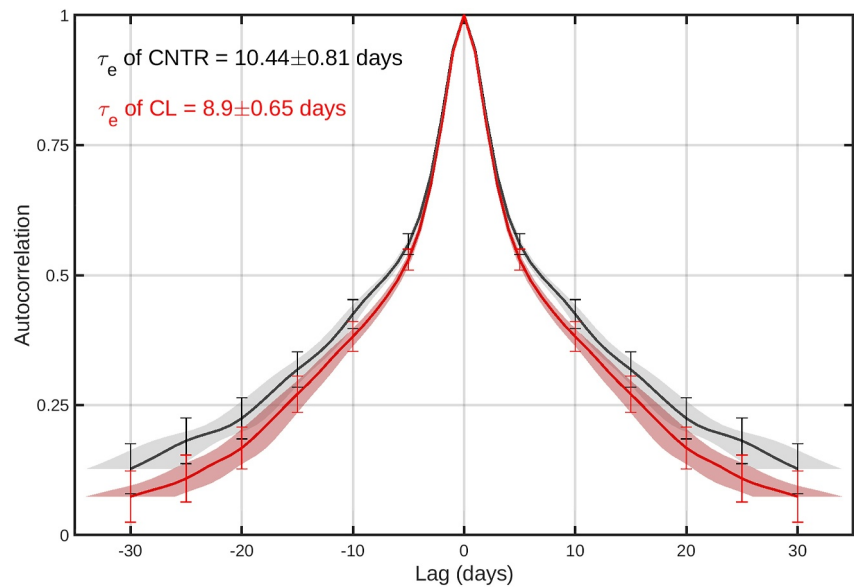


Figure 3. Autocorrelation of SAM index in CTRL (black) and CL (red) simulations. Shadings indicate the one standard deviation range of the decorrelation time scale τ and whiskers indicate the one standard deviation range of the autocorrelation at a given lag. These uncertainty ranges are estimated following the method of Gerber et al. (2008). The e-folding time (τ_e) of the SAM index for each case is labeled as well.

diabatic wave source was misinterpreted as part of the wave dissipation. The importance of the diabatic wave source term (wave activity dissipation term) as a positive (negative) feedback for the SAM has been confirmed with a similar feedback analysis using MERRA2 data set (Gelaro et al., 2017; Smith et al., 2024).

Decomposing the EMFC into the contributing components, we find that it is the enhanced diabatic feedback (Figure 5a) that increases the positive feedback in CTRL relative to CL. In the CL case, the baroclinic feedback appears to be enhanced to compensate the disabled CRE, but this positive feedback anomaly is offset by the enhanced negative feedback from the wave dissipation mechanism (Figure 4d), leaving little net feedback onto the SAM. Intriguingly, both the baroclinic and dissipation terms exhibit an oscillatory behavior at extended lags, a feature that may be linked to the propagation regime of the SAM. Further decomposing the diabatic effects into condensation, cloud, and clear-sky radiative heating, we may attribute the enhanced diabatic feedback to the changes in both condensation and cloud CRE (Figure 5a, pink and gray lines), the latter being dominated by the longwave component (red line). In the CL experiment the direct CRE plays no role in the SAM feedback during the positive lags, and the suppression of the CRE and condensational feedbacks is partially compensated by the clear-sky radiative feedback (Figure 6b). This is a good example of cloud modulation of SAM feedbacks through other diabatic processes, although how the interactive CRE enhances condensational heating while suppressing clear-sky radiation in the weeks after the SAM peaks remains an open question for future investigation.

3.2. Structure of the Diabatic Feedbacks

We further investigate the spatial and temporal structure of the feedbacks by performing a lagged correlation of the total diabatic wave source and the CRE LW component with the SAM index in CTRL. The result shows that both before and after the SAM index peaks, the total diabatic source provides a persistent wave source dipole straddling the mean jet (Figures 6a and 6c); this wave source dipole provides the wave activity that enhances the upper-tropospheric cross-jet wave propagation that is already established through the dry feedback mechanisms (see Burrows et al., 2017; Zurita-Gotor et al., 2014). The diabatic positive feedback to the SAM wind anomalies is dominated by the latent heating released in the anti-cyclonic sectors of the waves (Figure 6a), while the latent heating in the cyclonic sectors (Figure 6b) works to accelerate (decelerate) the zonal wind at the equatorward flank of the positive (negative) lobe of the SAM wind anomalies, propagating the zonal wind anomalies equatorward (i.e., against the poleward propagation; see also the cross-EOF analysis later).

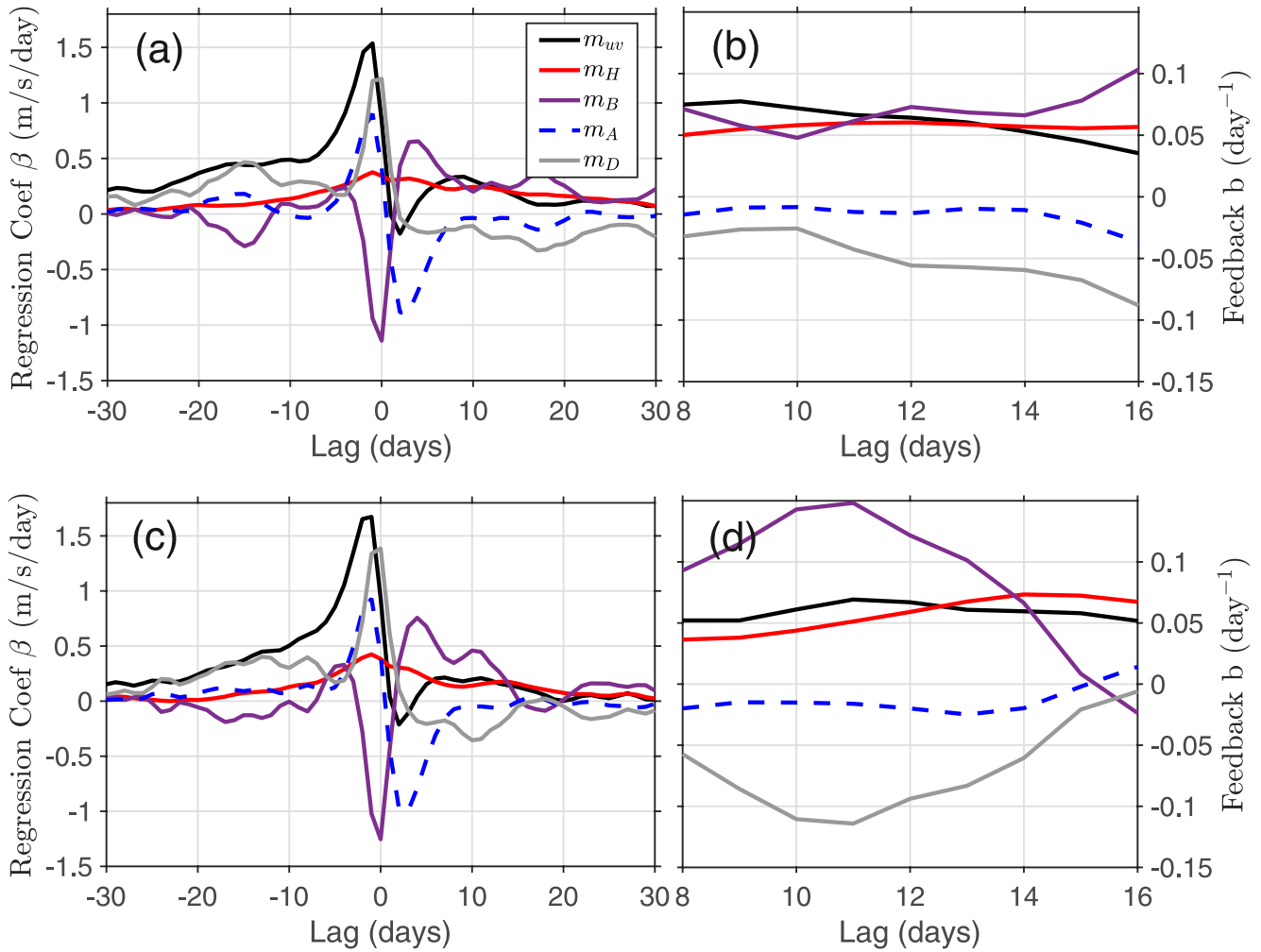


Figure 4. Lagged regression (a) and (c) of the wave activity budget terms to the SAM index and the related feedback parameters (b) and (d) (see main text for explanation) for CTRL (top) and CL (bottom) runs, respectively. Note that the feedback parameters in (b) and (d) are all significantly different from zero at 99% level based on a 10,000-trial Monte Carlo test except for m_A .

Like the total diabatic source, the positive SAM feedback from the CRE arises mainly from the anti-cyclonic sector of the waves (see Figures 6d–6f). Throughout the lifecycle of the SAM, the cyclonic and the anti-cyclonic sectors organize the cloud distribution in the storm track in a somewhat opposite manner (Figure 6d vs. Figure 6e) and the dominance of the cyclonic CRE gives way to the anticyclonic CRE after the SAM phase peaks. This transitional behavior of the LW CRE feedback may not be just a model behavior, as the same has been found from a similar analysis of the MERRA2 reanalysis data (see Figures 6a and 6d in Smith et al. (2024)). Note here that only the eddy component of the CRE is considered in the results shown in Figures 6d–6f; clouds can influence the annular mode dynamics indirectly through the zonal mean CRE, the midlatitude stratification and baroclinicity, and even the mean jet position.

The vertical structure of the upper-tropospheric diabatic wave sources during the feedback phase can be obtained by regressing them against the SAM index with a 10-day lag, and this is done with both the CTRL run and the MERRA2 reanalysis. Both the condensational and the clear sky heating sources project positively onto the dipolar wind structure of the SAM in both E3SM model (Figures 7a and 7d) and MERRA2 (Figures 7e and 7h), consistent with their positive feedback to the SAM in the analysis above. The regression patterns of MERRA2 are slightly shifted poleward compared to their E3SM counterparts, this is because the mean westerly jet in MERRA2 is located at 49.9°, about 2.3° more poleward than in E3SM (see the vertical lines in Figure 7). On the other hand, there is no resemblance in the patterns of the CRE wave sources between the two (compare Figures 7b and 7c to

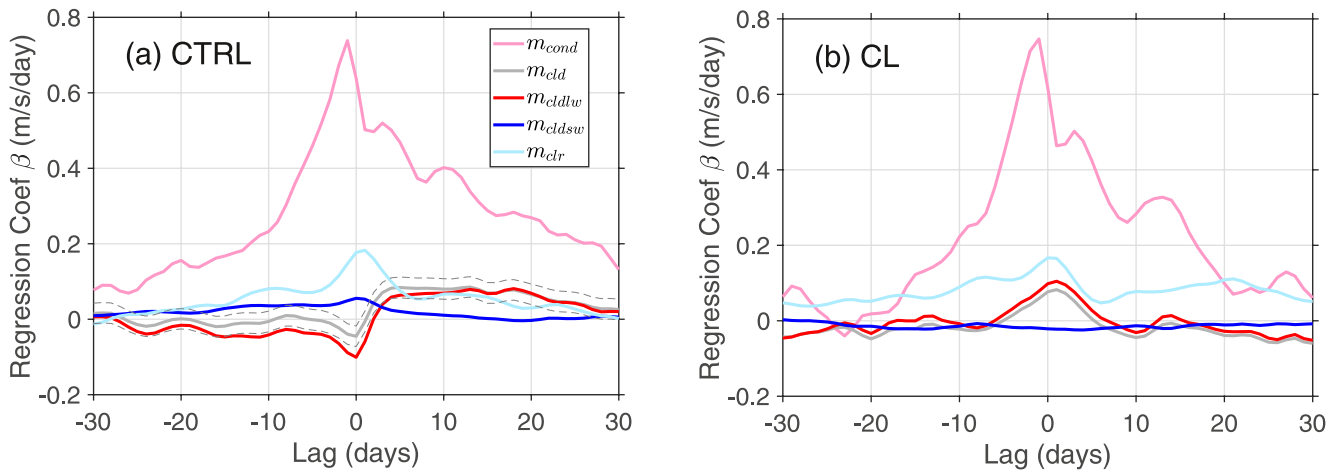


Figure 5. Lagged regression of the wave sources from different diabatic processes to the SAM index in CTRL (a) and CL (b). The pink, gray, red, blue, and light blue lines are for condensational heating (m_{cond}), total CRE (m_{cld}), longwave CRE (m_{cldlw}), shortwave CRE (m_{cldsw}), and clear-sky radiative heating (m_{clr}), respectively. The thin dashed lines in (a) indicate the 0.5th to 99.5th percentiles of the distribution of the regression coefficients computed from the 10,000 times of random sampling of the CRE momentum forcing. Other diabatic momentum forcings have uncertainty range of similar magnitude (not shown). Note that these regression curves are based on the original upper-tropospheric diabatic wave sources; they should be multiplied by a factor of 4/9 to compare with the regression coefficients in Figure 4.

Figures 7f and 7g), implying a much greater uncertainty in the cloud feedback to the SAM. Therefore, we only have limited confidence in the positive CRE feedback to the SAM. Given the complex spatial and temporal structure of the cloud field and the significant discrepancies between the E3SM model, the MERRA2 reanalysis, and observations (Li & Thompson, 2016; Wall et al., 2022), the questions of the robustness of the CRE feedback

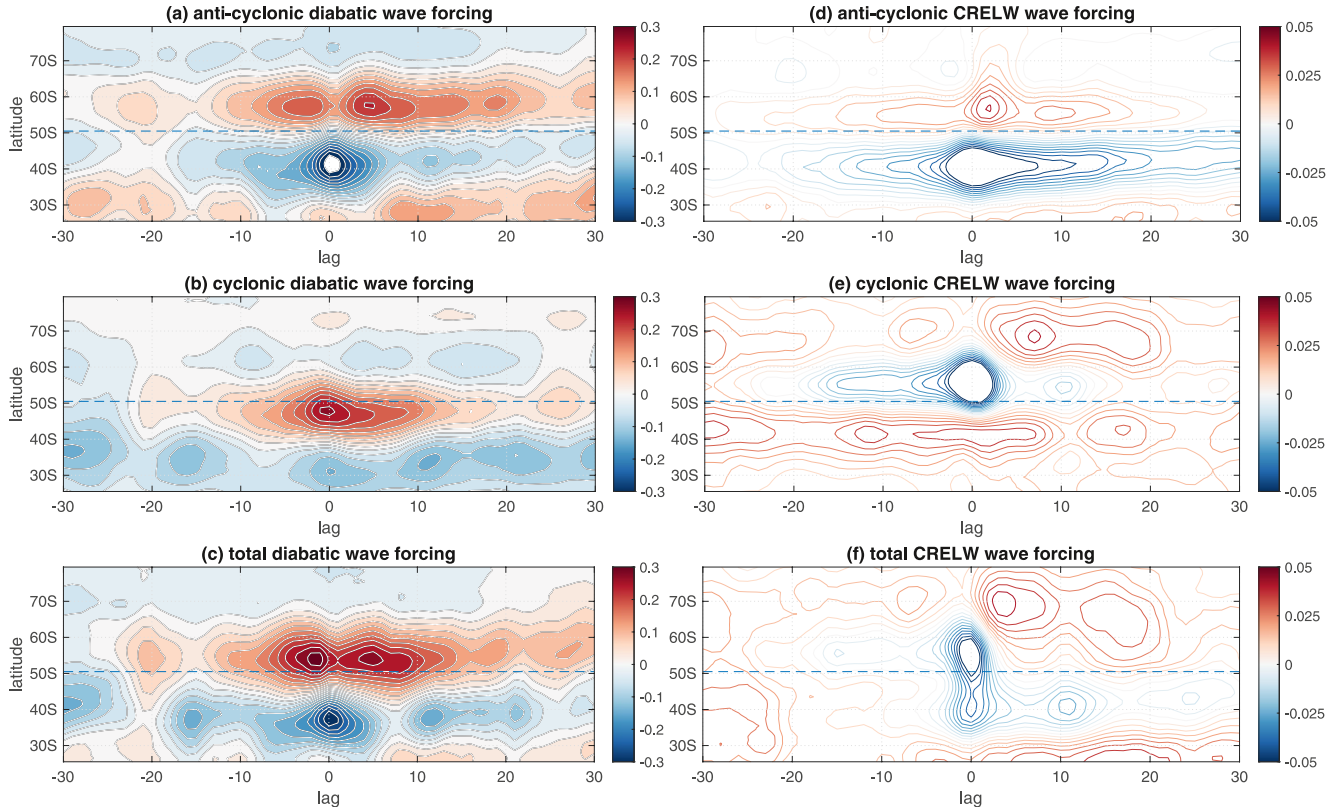


Figure 6. Lagged correlation of the wave activity source onto the SAM index. Left: for the total diabatic wave source; Right: for the CRE LW wave source. Positive lags for the SAM index leading the wave source of interest. The blue dashed line indicates the mean jet position at 48.8°S in CTRL, which also corresponds to the nodal latitude of the SAM wind anomalies. Unit is $\text{ms}^{-1} \text{day}^{-1}$.

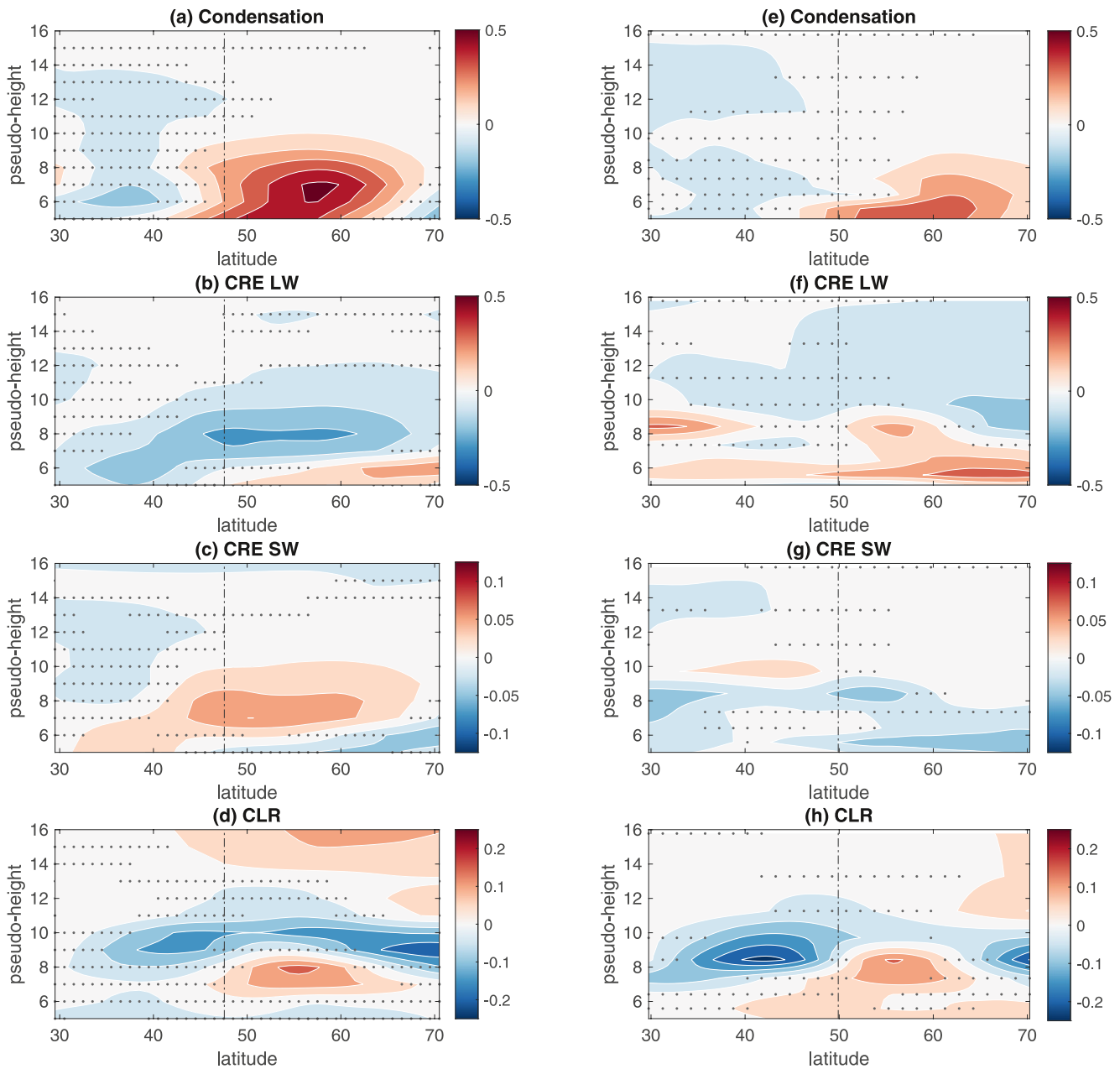


Figure 7. Regression of diabatic wave sources involved in the $\frac{f e \bar{h}}{\cos \phi} \frac{\partial}{\partial z} \left(\frac{\dot{Q}_e^{(k-1)z/H}}{c_p \partial \theta / \partial z} \right)$ term: (a) and (e) Condensation, (b) and (f) CRE LW, (c) and (g) CRE SW, and (d) and (h) clearsky heating (CLR), against the SAM index at lag 10. The left panels are for CTRL E3SM experiment and the right panels for MERRA2 reanalysis. Stippling indicates the areas where the regression is not confident as 95% level based on bootstrapping test. Unit: $\text{ms}^{-1} \text{day}^{-1}$ per std of the SAM index. The vertical line in each panel marks the position of the climatological mean westerly jet.

and the distinction of the relative roles of the direct CRE and indirect CRE are beyond the scope of the current study and are left to future investigations.

In addition to the sizable indirect CRE through the condensational heating term (Figure 6a, pink line), we cannot rule out another indirect effect of CRE—through the shift of the mean jet and the associated barotropic feedbacks. It is relatively established in annular mode literature that a more poleward jet position in the mean state tends to support a less persistent annular mode through dry dynamical feedbacks (e.g., Barnes & Hartmann, 2010; Burrows et al., 2017; Kidston & Gerber, 2010). Specifically, Barnes and Hartmann (2010) found that the e-folding time of the SAM decreases by 3 days per degree of poleward shift of the mean jet. The 1.2° jet shift

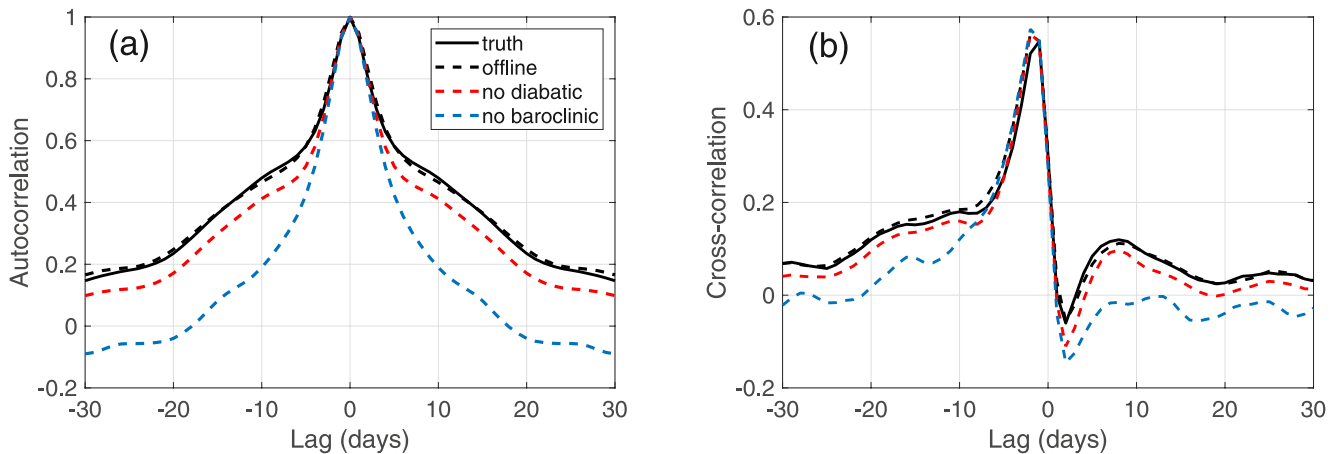


Figure 8. (a) Autocorrelation of the zonal index in CTRL and those based on the offline model simulations. (b) Cross-correlation between the zonal index and the EMFC simulated in CTRL and those based on the offline model simulations. In the offline models, the correlations from the integration using the full EMFC (m) is shown as the black dashed lines; the red dashed are and the blue dashed line are for the integrations with the diabatic term (m_H) and the baroclinic term (m_B) removed, respectively.

in CL compared to CTRL is more than enough to explain the ~ 1.5 days decrease in the SAM e-folding time. Therefore, we cannot attribute the reduced SAM persistence in CL exclusively to the CRE-related diabatic feedbacks.

3.3. Offline Model for the Diabatic Feedbacks

Given the above diagnostic result regarding the positive diabatic feedbacks of the SAM, we adopt a complementary offline modeling approach of Zurita-Gotor et al. (2014) to illustrate these feedbacks more explicitly. Treating Equation 4 as a conceptual model for the zonal index, we may integrate it in time with certain momentum or wave source of interest omitted and then examine the effect on the statistics of the zonal index. For example, comparing the case where the diabatic source (m_H) is omitted with the case where all the momentum and wave source terms are included would help to isolate the feedback effect of the diabatic source. We first tune the τ_f parameter in 4 to create a baseline case for the offline model, so that the simulated zonal index (z) closely approximates the statistics of the zonal index of CTRL. It turns out choosing a $\tau_f = 8.5$ days gives the best fit (compare the solid black line with the dashed black line in Figure 8). The offline integration without the diabatic source (m_H) indeed reduces the persistence of the zonal index and this is due to the reduction of the positive feedback at positive lags when the diabatic source is omitted (Figure 8, red dashed lines). The offline integration without the LW CRE source (m_{cldw}) reduces the persistence of the zonal index very marginally (hence not shown). Furthermore, the offline integration without the baroclinic source can eliminate the positive eddy feedback (Figure 8, blue dashed lines). These results are consistent with those from the direct diagnostic analysis above and the established understanding of the importance of the baroclinic feedback.

3.4. Propagating SAM

Caution must be exercised in interpreting the results from single EOF-based analysis, as evidenced by several recent studies (LH21; Sheshadri & Plumb, 2017; Smith et al., 2024). The standing dipole view of the SAM may be a reasonable first-order representation of the leading mode of the SH circulation variability; however, these recent studies suggest that the leading dynamical mode of the midlatitude wind variability is better viewed as a propagating pattern rather than a standing one. Relatedly, while exponential decay is appropriate for quantifying the predictability of red noise systems, it is inadequate for quantifying the predictability of propagating modes. The single EOF-based application of the fluctuation-dissipation theorem may also be a major source of error in estimating the magnitude of the zonal wind response to external forcing (Hassanzadeh & Kuang, 2016b; Ring & Plumb, 2008; Sheshadri & Plumb, 2017).

According to Lee et al. (2007), a rule of thumb for the existence of a stationary annular mode is a 2:1 ratio of the fractional variance explained by the first two EOFs (Lee et al., 2007). The fractional variances of the density-weighted vertical integration of the zonal wind explained by the leading two EOFs in CTRL are 41% and

Table 1

The Statistics of the EOFs and First POP Mode Diagnosed From CTRL and CL Experiments

Experiment	Var explained by EOF1 (%)	Var explained by EOF2 (%)	LHC	Decay time of DMD1 (days)	Period of DMD1 (days)
CTRL	41	33	−0.062	12.5	156
CL	40	35	−0.083	14.9	205

Note. The POP modes are computed using the DMD algorithm based on the projection time series of the zonal wind onto the leading two EOFs. The code used for the DMD analysis is from Bai et al. (2017, code accessible at <https://github.com/zhbai/cDMDc>).

33%, respectively, which is a much smaller ratio than 2:1. An even smaller ratio is found in the CL experiment (see Table 1). Thus, the leading two EOFs of the SH wind are most likely not independent. Moreover, it has been well known that the mid-latitude variability is governed by non-normal dynamics (e.g., Farrell & Ioannou, 1996; Navarra, 1993; Palmer, 1999), and for a non-normal system, EOFs may be strongly coupled to each other (e.g., Hassanzadeh & Kuang, 2016b). Therefore, single-EOF analysis may not be sufficient to capture the dynamics of the SAM variability and feedbacks, and a more advanced analysis tool is needed to capture the cross-EOF interactions and the feedback mechanisms involved.

To explore the cross-EOF interactions, we have performed a DMD analysis on the first two EOFs of the vertically integrated zonal wind (see Section 2). The resulting DMD mode (or the leading POP) picks up a propagation mode (corresponding to a pair of complex eigenvalues) of the SH zonal wind in both CTRL and CL, with a period of 156 days and a decay time of 12.5 days in the former and a period of 205 days and a decay time of 14.9 days in the latter. The LHCs in both cases are significantly less than zero (with an almost 0 p-value for both cases according to 10,000-trial Monte Carlo tests), indicating a well-defined propagation regime (Table 1). The increase of 31% in the propagation period in CL contributes negatively to the magnitude of the LHC if acting alone. However, according to Equation 8, it is both the period and the decay rate that jointly determine the LHC. It is important to note that a larger LHC magnitude does not necessarily imply greater predictability. Later in this subsection, we will further examine the predictability of the first DMD mode in CTRL and CL. As suggested in LH21, the enhanced oscillation in the propagating DMD mode in CL can be imprinted in the persistence of the SAM index, with the phase oscillation during the life cycle of the propagation being recast as an additional decay of the SAM index in the analysis based on a single EOF, reducing the persistence of the SAM index.

To diagnose the driving and feedback mechanisms in the propagation mode, we use a cross-EOF momentum budget analysis (see Figure 9), that is, we correlate the momentum source for EOF2 (i.e., the projection terms on the rhs of Equation 4) with the time series of EOF1, and vice versa for the time series of EOF2. For example, the momentum source for EOF1 due to diabatic heating is simply the projection of \mathcal{H} onto the normalized EOF1 pattern (i.e., the m_H term in Equation 4). We first inspect the overall effect of the EMFC (m_{uv}) and find that its role at different lags with respect to EOF1 (EOF2) (black lines in Figures 3a and 3b) corresponds well to what is found for the propagation regime of the zonal wind in LH21 (see their Figures 4e, 4f, 7e, and 4f). Both the correlations at short negative lags and the extended positive lags are significant at 99% confidence based on bootstrapping sampling (the 0.5% and 99.5% percentiles of the m_{uv} regressions based on 10,000 samples are shown by the dashed black lines). Decomposing m_{uv} into its contributing components confirms that the wave activity dissipation (\mathcal{D} , gray lines) due to wave breaking is the dominant driving mechanism for the propagation, while providing positive feedback to the propagation at positive lags. This is consistent with the critical level feedback mechanism of Lee et al. (2007) for the jet propagation in an idealized dry model: the negative wind anomalies are initiated by breaking of waves that originate in midlatitudes, the homogenization of the potential vorticity (PV) results in positive wind anomalies at its poleward edge. Subsequently, the equatorward radiation of the mid-latitude waves feel a poleward shifted critical level, which leads to wave breaking at more poleward latitudes and a more poleward zone of PV homogenization. This feedback cycle continues, enabling the poleward propagation of the zonal wind anomalies. To the best of our knowledge this mechanism has not been confirmed and quantified in realistic atmospheric models until this work. On the other hand, the diabatic wave source (\mathcal{H}) acts as an overall impediment to poleward propagation. Interestingly, the dissipation term appears to pass on its driving role to the baroclinic term (\mathcal{B}) after EOF1 peaks (see Figures 9a and 9c), while this relay relationship is less clear for EOF2 (cf. Figures 9b and 9d). It is worth noting that all these phase relationships between the states of the zonal wind and the momentum source terms are qualitatively consistent with those found in the MERRA2 reanalysis in Smith

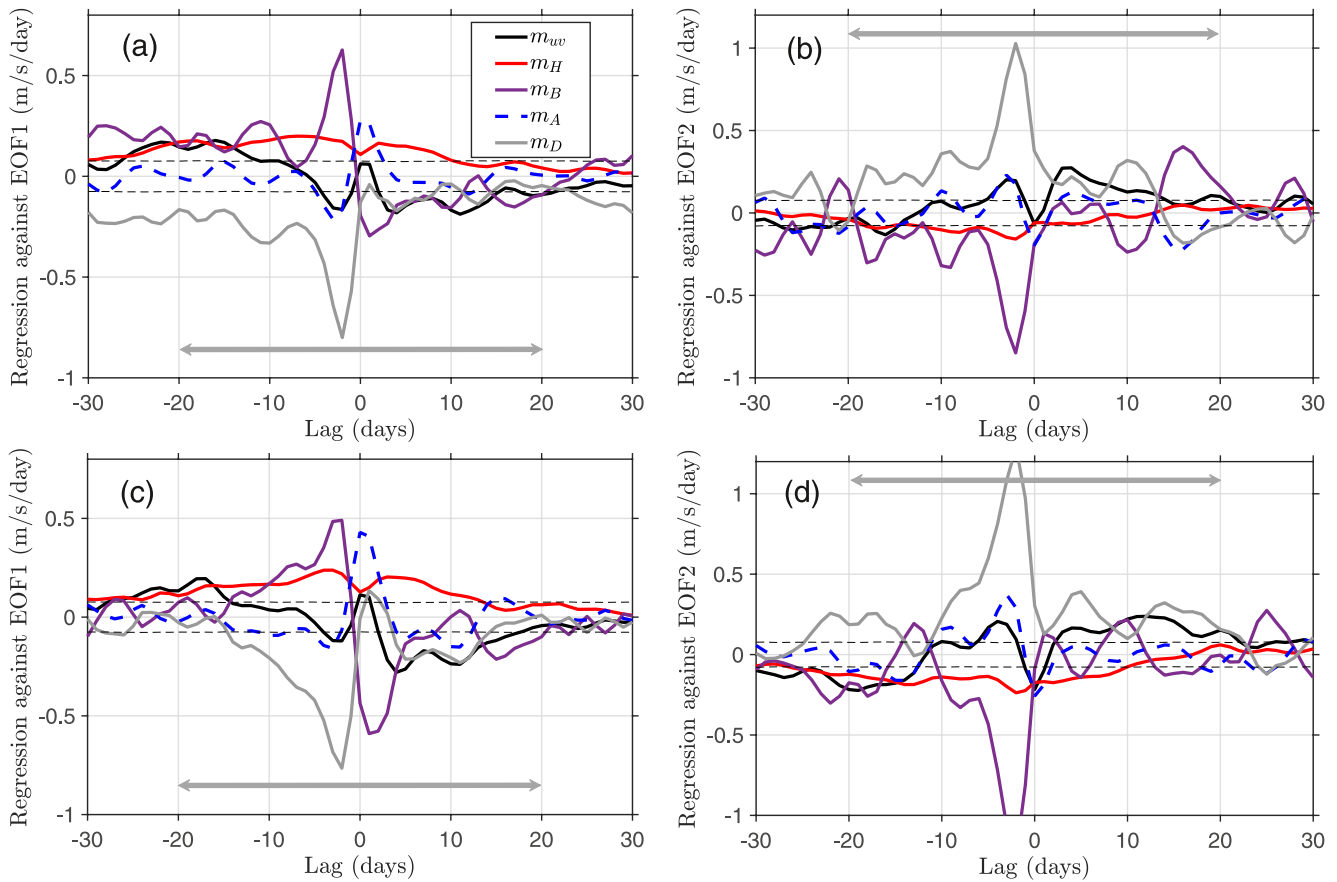


Figure 9. Lagged regression of EMFC (m_{wv}) and its contributing components against the time series of z_1 (projection coefficient on EOF1, panel a) and z_2 (projection coefficient on EOF2, panel b). Since the sign convention is such that poleward propagation of a positive zonal wind anomaly starting from the subtropics represents a progression of $-EOF1 \rightarrow +EOF2 \rightarrow +EOF1 \rightarrow -EOF2$, negative regression at the short negative lags against EOF1 indicates a positive driving mechanism for the poleward propagation, and negative regression at positive lags (when the zonal wind anomalies lead the feedbacks) implies positive feedback to sustain the propagation in panel (a), and vice versa for the regression against EOF2 in panel (b). Panels (c) and (d) are the same as (a) and (b), but for the CL experiments. The double-angled line in each panel indicates the lag range where a negative (positive) correlation with EOF1 (EOF2) wind implies a positive contribution to the poleward propagation of a hypothetical 160-day periodicity.

et al. (2024). The tendency for cancellation between the EMFC and the baroclinic term at shorter timescales has also been found in several previous studies (Boljka et al., 2018; Sparrow et al., 2009; Zurita-Gotor et al. (2014).

Disabling the CRE in CL appears to enhance the driving mechanism through wave dissipation prior to the peak phase of EOF2 and the associated positive feedback at positive lags (Figure 9d, gray line). However, the increase in the feedback through the total EMFC (c.f. black lines in Figures 9c and 9d) is marginal at best compared to CTRL, thanks to the slight enhancement of the diabatic term as the main impedance to the propagation (red lines). Comparing between CL and CTRL, it is difficult to establish the significance of the changes in the driving and feedback mechanisms in the propagation mode in a rigorous statistical sense. Looking into the CRE in CTRL (Figure 10), we note that the LW CRE acts as a brake on the poleward propagation of the zonal wind anomalies: immediately after the initiation of the propagation by the wave breaking, the cloud fields are configured such that the EOF2 (EOF1) forcing on the EOF1 (EOF2) wind due to m_{clw} is positive (negative) around lag 2, impeding the poleward propagation according to the sign convention of the EOFs (see the caption of Figure 9). Therefore, disabling the braking effect of the interactive CRE on propagation in CL should promote the propagation regime of the SAM. Taken together, a consistent picture about the CRE feedback in the E3SM appears to emerge: CRE acts as a positive feedback to EOF1, disabling CRE reduces the persistence and the variance of the single EOF-based SAM index, but somewhat boosts the fractional variance in EOF2. Disabling CRE also boosts the cross-EOF interaction, although the exact mechanisms and the robustness thereof remain an open question. In the cross-EOF analysis framework of LH21, the k_{11} and k_{22} parameters for the self-feedback for EOF1 and EOF2,

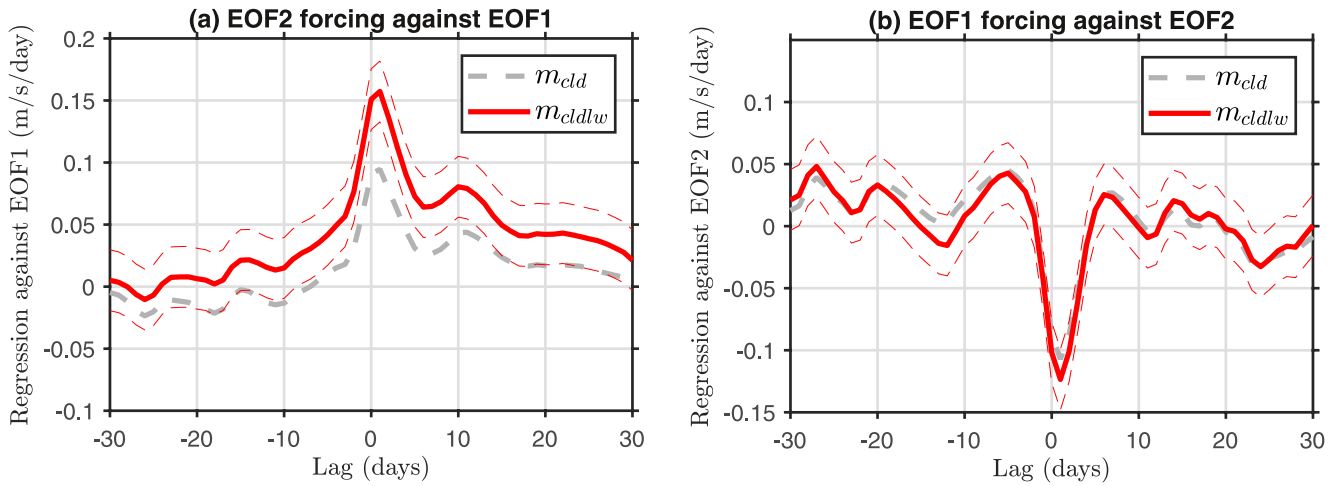


Figure 10. Same as Figures 9a and 9b Except for the wave source due to CRE (gray) and its LW component (red). Note that the magnitude here should be multiplied by a factor of 4/9 to compare with that shown in Figure 9. The thin red dashed lines indicate the 0.5th to 99.5th percentiles of the distribution of the regression coefficients based on 10,000 random samples of the m_{cldlw} time series.

respectively, are closer to each other, while the cross-EOF interaction measured by $k_{12}k_{21}$ increases in the LHC criterion. As a result, the LHC is better satisfied in CL than in CTRL and the leading propagation mode represented by the first DMD mode (POP1) becomes less damped in CL (see Table 1).

We next try to quantify the change in the annual mode predictability due to disabling the interactive CRE. A predictability measure based on information-theoretical principles has been devised for system investigated here (Schneider & Griffies, 1999); its general form is formulated as

$$1 - \frac{\text{tr}\mathbf{G}_\tau}{n} = \frac{1}{n} \sum_{k=1}^n \sigma_k^2(\mathbf{W}_\tau), \quad (9)$$

and it equals to its lower limit

$$\frac{1}{n} \sum_{k=1}^n e^{2\text{Re}\lambda_k(\mathbf{A})\tau}, \quad (10)$$

when the stochastic forcing of the system is uncorrelated in normal mode space. \mathbf{G}_τ is the predictive information matrix, $\mathbf{W}_\tau = \mathbf{C}_\infty^{-1/2} \mathbf{K}_\tau \mathbf{C}_\infty^{1/2}$ is the matrix of the state-propagator for the whitened state variable (by the square root of the climatological prediction error covariance matrix \mathbf{C}_∞), \mathbf{A} is the dynamic matrix of the system, σ_k indicates the singular values of \mathbf{W}_τ , and $\lambda_k(\mathbf{A})$ the eigen values of \mathbf{A} . See Tippett and Chang (2003) for details on the derivation of the predictability measures and their computation. In our case, once the matrix \mathbf{K} is estimated from the DMD analysis, we can use these predictability measures to quantify the predictability of the leading DMD mode in CTRL and CL. Specifically, the climatological error covariance matrix and the state-propagator matrix are computed based on the time series simulated by integrating a system governed by a dynamics $\mathbf{A} \approx \frac{1}{\tau_{\text{DMD}}} (\mathbf{K} - \mathbf{I})$, where \mathbf{K} is the matrix operator for z_1 and z_2 estimated using DMD at lag $\tau_{\text{DMD}} = 22$ days, and forced by random white noise whose magnitude is estimated based on the projection time series of m_{uv} on the EOFs. As astutely pointed out by Tippett and Chang (2003), the predictability measures formulated by 9 and 10 are independent of the magnitude of the forcing. The computed predictabilities of the two-EOF system extracted from CTRL and CL using DMD are shown in Figure 11. Consistent with the weaker decay rate of the DMD1 in CL, the DMD1 there is also more predictable compared to CTRL (compare the dashed pink line to the black line in Figure 11), despite the fact that the e-folding time of EOF1 is shorter in CL than in CTRL. A more comprehensive evaluation of the enhanced predictability due to the propagation regime is underway and the results will be reported elsewhere.

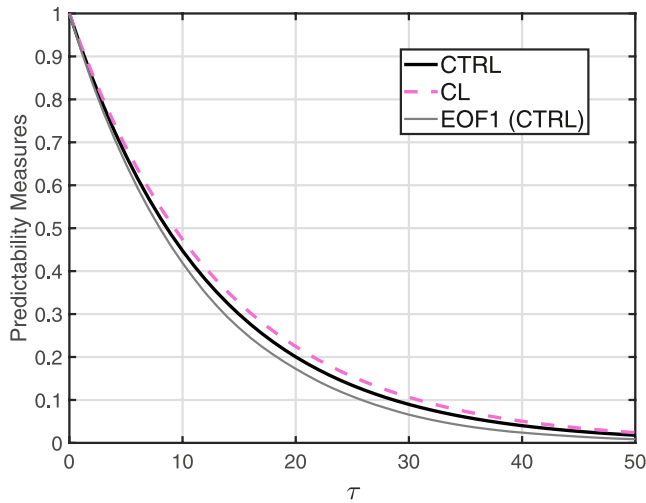


Figure 11. The information-based predictability measures (using Equation 9) for the leading DMD mode of the 2-EOF system under uncorrelated noise forcing in CTRL (solid black) and CL (dashed pink). The R^2 (square of autocorrelation) of the stochastically forced z_1 time series is shown in the solid gray line as a reference. Considering correlated stochastic forcing results in only a minimal change in the predictability (not shown), suggesting that the different predictability between CTRL and CL is mainly the result of the difference in the operating dynamics.

4. Summary and Discussion

In this study, we isolate and quantify the interactive CRE feedback to the SAM through implementing the cloud locking technique to DOE's E3SM atmospheric model and perform a wave activity and zonal momentum budget-based feedback analysis. SAM-organized structures in cloud and the associated radiative heating effect have been examined in the literature, however the dynamical feedback from the CRE to the SAM remains elusive up to now. While both the cloud locking experiment and the feedback analysis here suggest a positive CRE feedback, the magnitude of the CRE feedback identified by both methods appears to be at most compared to the feedbacks from the dry and other diabatic processes. In addition, the indirect CRE effects through the interaction with other dynamical and thermodynamical processes appear to play as important a role as the direct CRE in the life cycle of the SAM. This study also demonstrates that cloud locking, to the extent that it does not cause significant drift in the climate state, is a feasible modeling technique for investigating the CRE feedback in the atmosphere. Given the inextricable coupling between clouds and other radiative and even dynamical processes, we recommend interrogating the interactive CRE as a whole using the locking technique rather than relying solely on the budget-based diagnostic approach.

Consistent with a companion study (Smith et al., 2024), we found that the total diabatic heating is a significant wave source for the positive feedback of the SAM. During the positive phase of the SAM, the diabatic heating (primarily the condensational heating and the clear sky radiative heating) in the anticyclonic sectors of the midlatitude storm track has a somewhat opposite phase relationship with the upper-troposphere potential vorticity anomalies between the equatorward and the poleward flanks of the mean jet, resulting in a positive diabatic wave source poleward of the jet and a negative wave source equatorward of the jet. This wave source dipole anchors an equatorward flux of wave activity in the upper troposphere, contributing to the maintenance of the positive phase of the SAM. The agreement between the results of the E3SM model and the MERRA2 reanalysis in Smith et al. (2024) gives us confidence in the positive diabatic feedback in the SAM. On the other hand, the CRE, both the direct CRE from the wave activity budget and the total interactive CRE extracted from cloud locking experiment, only plays a weak positive feedback role in the SAM, and the enhancement of persistence of the SAM index due to the interactive CRE is barely detectable. Although both the E3SM model and the MERRA2 reanalysis agree on the sign of the CRE feedback, the spatial structures of the cloud distribution during the feedback phase are very different between the model and the reanalysis. In addition, the hindering effect of CRE on the poleward propagation regime of SAM is not found in the cross-EOF analysis of the MERRA2 reanalysis.

Recent studies from a multi-EOF perspective indicate that the single-EOF approach does not fully capture the annular mode of the zonal jet variability (LH21, Lubis & Hassanzadeh, 2023; Smith et al., 2024). Our cross-EOF analysis and the DMD analysis based on two EOFs may provide a more comprehensive representation of the spatiotemporal characteristics and the predictability of the annular mode, especially when it is in a propagation regime. Our analysis reveals that the eddy diabatic processes as a whole act to hinder the poleward propagation of the SAM wind anomalies, with the CRE (both direct and interactive) being a part of this role. As such, disabling the interactive CRE in the CL simulation enhances the propagation regime of the annular mode. The more persistent propagation mode in CL compared to CTRL also implies that the dynamically organized SH wind variability might be more predictable in CL than in CTRL, despite the longer persistence of the single EOF-based SAM in the latter. These seemingly contradictory results can be reconciled by the possibility that the single EOF analysis misinterprets the phase reversal in the propagating mode as an accelerated decay. How this new propagation perspective on the annular mode may affect our understanding of the predictability of the midlatitude wind variability can be an interesting topic for future investigation.

Most of the results of this study have been confirmed by analysis of the MERRA2 data in a companion study (Smith et al., 2024). However, the dominant propagation period found in MERRA2 from 2005 to 2019 is about 60 days, which is much shorter than that associated with the E3SM simulations, suggesting that the precise period

of the leading propagation mode is the result of an intricate orchestration between these adiabatic and diabatic processes, as well as their relationships with the mean jet configuration (e.g., Son & Lee, 2007). Given the fact that the processes that determine the diabatic heating and CRE are often parameterized in atmospheric models and are thus an important source of model uncertainty, any inaccuracy in the representation of these processes is likely to manifest itself in the spatial and temporal characteristics of the leading mode of the westerly jet variability, underscoring the challenges for climate models to accurately capture these characteristics. Future efforts should focus on inter-model comparisons of CRE-denial experiments with different models to build consensus on the dynamical feedback of CRE, and on model-reanalysis-observation comparisons to improve the associated process-level understanding.

Appendix A: The Relationship Between LHC and the Decay Rate and Period of the Leading DMD Mode

The DMD-learned matrix operator \mathbf{K} propagates the system at time increments of τ is related to the dynamic operator \mathbf{A} as follows:

$$\mathbf{K} = e^{\mathbf{A}\tau} \quad (\text{A1})$$

Diagonalizing the propagator operator gives

$$\mathbf{V}\mathbf{\Lambda}_K\mathbf{V}^{-1} = \mathbf{V}e^{\mathbf{\Lambda}_A\tau}\mathbf{V}^{-1}$$

where \mathbf{V} and $\mathbf{\Lambda}_K$ contains the eigenvectors and eigenvalues of \mathbf{K} ; $\mathbf{\Lambda}_A$ is a diagonal matrix whose diagonal entries are the eigenvalues of \mathbf{A} . Particularly, the eigenvalues of \mathbf{K} and \mathbf{A} are related:

$$\lambda_K = e^{\lambda_A\tau} \quad (\text{A2})$$

where λ_A determines the temporal characteristics of the leading DMD mode of the two-EOF system. Equalizing the imaginary part, we have

$$\lambda_K^I = e^{\lambda_A^R\tau} \sin \lambda_A^I\tau \quad (\text{A3})$$

Using the definition of the LHC (i.e., $\text{LHC} \equiv -4\lambda_K^{I2}$, LH21) and denoting the decay rate and the period of the propagation DMD mode as $\sigma = -\lambda_A^R$ and $T \equiv 2\pi/\lambda_A^I$, respectively, we yield

$$\text{LHC} = -4e^{-2\sigma\tau} \sin^2(2\pi T^{-1}\tau) \quad (\text{A4})$$

Acknowledgments

This study was supported by Office of Science, U.S. Department of Energy Biological and Environmental Research (BER) as part of the Regional and Global Model Analysis program area. We thank the two reviewers for their valuable suggestions that help improve our study and the manuscript. The Pacific Northwest National Laboratory (PNNL) is operated for DOE by Battelle Memorial Institute under contract DE-AC05-76RLO1830. This research was performed using BER Earth System Modeling program's Compy computing cluster located at Pacific Northwest National Laboratory. Additional analyses were performed using resources of the National Energy Research Scientific Computing Center, a DOE Office of Science User Facility supported by the Office of Science of the U.S. Department of Energy under Contract No. DE-AC02-05CH11231. This work also benefits from constructive discussion with Kevin Grise.

which is Equation 8 in the main text.

Data Availability Statement

The data used for the main conclusions in this study has been released and is publicly accessible at https://portal.nersc.gov/cfs/m1867/jianlu/SAM_CL_data_sharing/. The code used for the main conclusions of this study can be also made available upon the request to the lead author.

References

- Bai, Z., Kaiser, E., Proctor, J. L., Kutz, J. N., & Brunton, S. L. (2017). Dynamic mode decomposition for compressive system identification. *AIAA Journal*, 58(2), 561–574. <https://doi.org/10.2514/1.J057870>
- Barnes, E. A., & Hartmann, D. L. (2010). Testing a theory for the effect of latitude on the persistence of eddy-driven jets using CMIP3 simulations. *Geophysical Research Letters*, 37(15), L15801. <https://doi.org/10.1029/2010GL044144>
- Benedict, J. J., Lee, S., & Feldstein, S. B. (2004). Synoptic view of the North Atlantic Oscillation. *Journal of the Atmospheric Sciences*, 61(2), 121–144. [https://doi.org/10.1175/1520-0469\(2004\)061<0121:svotma>2.0.co;2](https://doi.org/10.1175/1520-0469(2004)061<0121:svotma>2.0.co;2)
- Boljka, L., Shepherd, T. G., & Blackburn, M. (2018). On the coupling between barotropic and baroclinic modes of extratropical atmospheric variability. *Journal of the Atmospheric Sciences*, 75(6), 1853–1871. <https://doi.org/10.1175/jas-d-17-0370.1>

- Bracegirdle, T. J., Holmes, C. R., Hosking, J. S., Marshall, G. J., Osman, M., Patterson, M., & Rackow, T. (2020). Improvements in circumpolar Southern hemisphere extratropical atmospheric circulation in CMIP6 compared to CMIP5. *Earth and Space Science*, 7(6), e2019EA001065. <https://doi.org/10.1029/2019ea001065>
- Burrows, D. A., Chen, G., & Sun, L. (2017). Barotropic and baroclinic eddy feedbacks in the midlatitude jet variability and responses to climate change—like thermal forcings. *Journal of the Atmospheric Sciences*, 74(1), 111–132. <https://doi.org/10.1175/jas-d-16-0047.1>
- Ceppi, P., & Hartman, D. L. (2016). Clouds and the atmospheric circulation response to warming. *Journal of Climate*, 29(2), 783–799. <https://doi.org/10.1175/JCLI-D-15-0394.1>
- Chen, G., Lu, J., & Sun, L. (2013). Delineating the eddy-zonal flow interaction in the atmospheric circulation response to climate forcing: Uniform SST warming in an idealized aqua-planet model. *Journal of the Atmospheric Sciences*, 70(7), 2214–2233. <https://doi.org/10.1175/jas-d-12-0248.1>
- Chen, G., & Plumb, R. A. (2009). Quantifying the eddy feedback and the persistence of the zonal index in an idealized atmospheric model. *Journal of the Atmospheric Sciences*, 66(12), 3707–3720. <https://doi.org/10.1175/2009JAS3165.1>
- Chen, G., Zhang, P., & Lu, J. (2020). Sensitivity of the latitude of the westerly jet stream to climate forcing. *Geophysical Research Letters*, 47(4), e2019GL086563. <https://doi.org/10.1029/2019GL086563>
- Farrell, B. F., & Ioannou, P. J. (1996). Generalized stability theory. Part I: Autonomous operators. *Journal of the Atmospheric Sciences*, 53(23), 3541–3555. [https://doi.org/10.1175/1520-0469\(1996\)053<3541:mozivi>2.0.co;2](https://doi.org/10.1175/1520-0469(1996)053<3541:mozivi>2.0.co;2)
- Feldstein, S. B., & Lee, S. (1996). Mechanisms of zonal index variability in an aquaplanet GCM. *Journal of the Atmospheric Sciences*, 53(23), 3541–3555. [https://doi.org/10.1175/1520-0469\(1996\)053<3541:mozivi>2.0.co;2](https://doi.org/10.1175/1520-0469(1996)053<3541:mozivi>2.0.co;2)
- Franzke, C., Lee, S., & Feldstein, S. B. (2003). Is the North Atlantic Oscillation a breaking wave? *Journal of the Atmospheric Sciences*, 61(2), 145–160. [https://doi.org/10.1175/1520-0469\(2004\)061<0145:itnaoa>2.0.co;2](https://doi.org/10.1175/1520-0469(2004)061<0145:itnaoa>2.0.co;2)
- Gelaro, R., McCarty, W., Suárez, M. J., Todling, R., Molod, A., Takacs, L., et al. (2017). The Modern-Era Retrospective Analysis for Research and Applications, Version 2 (MERRA-2). *Journal of Climate*, 30(14), 5419–5454. <https://doi.org/10.1175/JCLI-D-16-0758.1>
- Gerber, E., Voronin, P. S., & Vallis, G. K. (2008). Testing the annular mode autocorrelation time scale in simple atmospheric general circulation models. *Monthly Weather Review*, 136(4), 1523–1536. <https://doi.org/10.1175/2007mwr2211.1>
- Gerber, E. P., & Vallis, G. K. (2005). A stochastic model for the spatial structure of annular patterns of variability and the North Atlantic Oscillation. *Journal of Climate*, 18(12), 2102–2118. <https://doi.org/10.1175/jcli3337.1>
- Golaz, J., Caldwell, P. M., Van Roekel, L. P., Petersen, M. R., Tang, Q., Wolfe, J. D., et al. (2019). The DOE E3SM coupled model version 1: Overview and evaluation at standard resolution. *Journal of Advances in Modeling Earth Systems*, 11(7), 2089–2129. <https://doi.org/10.1029/2018ms001603>
- Grise, K. M., Medeiros, B., Benedict, J. J., & Olson, J. G. (2019). Investigating the influence of cloud radiative effects on the extratropical storm tracks. *Geophysical Research Letters*, 46(13), 7700–7707. <https://doi.org/10.1029/2019GL083542>
- Harrop, B. E., Lu, J., Leung, L. R., Lau, W. K. M., Kim, K.-M., Medeiros, B., et al. (2024). An overview of cloud-radiation denial experiments for the Energy Exascale Earth System Model version 1. EGU sphere. <https://doi.org/10.5194/egusphere-2023-1555>
- Hassanzadeh, P., & Kuang, Z. (2016a). The linear response function of an idealized atmosphere. Part I: Construction using Green's functions and applications. *Journal of the Atmospheric Sciences*, 73(9), 3423–3439. <https://doi.org/10.1075/JAS-D-15-0388.1>
- Hassanzadeh, P., & Kuang, Z. (2016b). The linear response function of an idealized atmosphere. Part II: Implication for the practical use of the Fluctuation-Dissipation Theorem and the role of operator nonnormality. *Journal of the Atmospheric Sciences*, 73(9), 3441–3452. <https://doi.org/10.1075/JAS-D-16-0099.1>
- Hassanzadeh, P., & Kuang, Z. (2019). Quantifying the annular mode dynamics in an idealized atmosphere. *Journal of the Atmospheric Sciences*, 76(4), 1107–1124. <https://doi.org/10.1075/JAS-D-18-0268.1>
- Huang, C. S. Y., & Nakamura, N. (2017). Local wave activity budgets of the wintertime Northern Hemisphere: Implication for the Pacific and Atlantic storm tracks. *Geophysical Research Letters*, 44(11), 5673–5682. <https://doi.org/10.1002/2017gl037376>
- Ioannou, P. J. (1995). Nonnormality increases variance. *Journal of the Atmospheric Sciences*, 52(8), 1155–1158. [https://doi.org/10.1175/1520-0469\(1995\)052<1155:niv>2.0.co;2](https://doi.org/10.1175/1520-0469(1995)052<1155:niv>2.0.co;2)
- Kidston, J., & Gerber, E. P. (2010). Intermodel variability of the poleward shift of the austral jet stream in the CMIP3. *Geophysical Research Letters*, 37(9), L09708. <https://doi.org/10.1029/2010GL042873>
- Lee, S., Son, S.-W., Grise, K., & Feldstein, S. B. (2007). A mechanism for the poleward propagation of zonal mean flow anomalies. *Journal of the Atmospheric Sciences*, 64(3), 849–868. <https://doi.org/10.1175/jas3861.1>
- Li, Y., & Thompson, D. W. J. (2016). Observed signatures of the barotropic and baroclinic annular modes in cloud vertical structure and cloud radiative effects. *Journal of Climate*, 29(13), 4723–4740. <https://doi.org/10.1175/jcli-d-15-0692.1>
- Li, Y., Thompson, D. W. J., Bony, S., & Merlis, T. M. (2019). Thermodynamic control on the poleward shift of the extratropical jet in climate change simulations: The role of rising high clouds and their radiative effects. *Journal of Climate*, 32(3), 917–934. <https://doi.org/10.1175/JCLI-D-19-0758.1>
- Liu, S., Staten, P. W., & Kahn, B. H. (2020). Improved detection of interannual cloud variability over the Southern Hemisphere using legacy satellites. *Journal of Climate*, 33(19), 8225–8236. <https://doi.org/10.1175/JCLI-D-18-0417.1>
- Lorenz, D. J. (2014). Understanding midlatitude jet variability and change using Rossby wave chromatography: Poleward-shifted jets in response to external forcing. *Journal of the Atmospheric Sciences*, 71(7), 2370–2389. <https://doi.org/10.1175/JAS-D-13-0200.1>
- Lorenz, D. J. (2022). Dynamics of the transient negative eddy response to zonal-mean zonal wind variations. *Journal of the Atmospheric Sciences*, 80(2), 593–610. <https://doi.org/10.1175/jas-d-22-0084.1>
- Lorenz, D. J. (2023). A simple mechanistic model of wave-mean flow feedbacks, poleward jet shifts, and the annular mode. *Journal of the Atmospheric Sciences*, 81(2), 549–568. <https://doi.org/10.1175/jas-d-22-0056.1>
- Lorenz, D. J., & Hartmann, D. L. (2001). Eddy-zonal flow feedback in the Southern Hemisphere. *Journal of the Atmospheric Sciences*, 58(21), 3312–3327. [https://doi.org/10.1175/1520-0469\(2001\)058<3312:ezffit>2.0.co;2](https://doi.org/10.1175/1520-0469(2001)058<3312:ezffit>2.0.co;2)
- Lubis, S. W., & Hassanzadeh, P. (2021). An eddy-zonal flow feedback model for propagating annular modes. *Journal of the Atmospheric Sciences*, 78(1), 249–267. <https://doi.org/10.1175/JAS-D-20-0214.1>
- Lubis, S. W., & Hassanzadeh, P. (2023). The intrinsic 150-day periodicity of the Southern Hemisphere extratropical large-scale atmospheric circulation. *AGU Advances*, 4(3), e2022AV000833. <https://doi.org/10.1029/2022AV000833>
- Lubis, S. W., Huang, C. S. Y., & Nakamura, N. (2018). Role of finite-amplitude eddies and mixing in the life cycle of stratospheric sudden warmings. *Journal of the Atmospheric Sciences*, 75(11), 3987–4003. <https://doi.org/10.1175/JAS-D-18-0138.1>
- Lutsko, N. J., & Hell, M. C. (2021). Moisture and the persistence of annular modes. *Journal of the Atmospheric Sciences*, 78, 3951–3964. <https://doi.org/10.1175/JAS-D-21-0055.1>

- Ma, D., Hassanzadeh, P., & Kuang, Z. (2017). Quantifying the eddy-jet feedback strength of the annular mode in an idealized GCM and reanalysis data. *Journal of the Atmospheric Sciences*, 75(2), 393–407. <https://doi.org/10.1175/JAS-D-16-0157.1>
- Middlemas, E. A., Kay, J. E., Medeiros, B. M., & Maroon, E. A. (2019). Quantifying the influence of cloud radiative feedbacks on Arctic surface warming using cloud locking in an Earth system model. *Geophysical Research Letters*, 47(15), 1–9. 2020. <https://doi.org/10.1029/2020GL089207>
- Nakamura, N., & Solomon, A. (2010). Finite-amplitude wave activity and mean flow adjustments in the atmospheric general circulation. Part I: Quasigeostrophic theory and analysis. *Journal of the Atmospheric Sciences*, 67(12), 3967–3983. <https://doi.org/10.1175/2010JAS3503.1>
- Nakamura, N., & Zhu, D. (2010). Finite-amplitude wave activity and diffusive flux of potential vorticity in Eddy-mean flow interaction. *Journal of the Atmospheric Sciences*, 67(9), 2701–2716. <https://doi.org/10.1175/2010jas3432.1>
- Navarra, A. (1993). A new set of orthonormal modes for linearized meteorological problems. *Journal of the Atmospheric Sciences*, 50(16), 2569–2583. [https://doi.org/10.1175/1520-0469\(1993\)050<2569:ansoom>2.0.co;2](https://doi.org/10.1175/1520-0469(1993)050<2569:ansoom>2.0.co;2)
- Nie, Y., Zhang, Y., Chen, G., Yang, X.-Q., & Burrows, D. A. (2014). Quantifying barotropic and baroclinic eddy feedbacks in the persistence of the Southern Annular Mode. *Geophysical Research Letters*, 41(23), 8636–8644. <https://doi.org/10.1002/2014GL062210>
- Palmer, T. N. (1999). A nonlinear dynamical perspective on climate predictability. *Journal of Climate*, 12(2), 575–591. [https://doi.org/10.1175/1520-0442\(1999\)012<0575:andpoc>2.0.co;2](https://doi.org/10.1175/1520-0442(1999)012<0575:andpoc>2.0.co;2)
- Papavasileiou, G., Voigt, A., & Knippertz, P. (2020). The role of observed cloud-radiative anomalies for the dynamics of the North Atlantic Oscillation on synoptic time-scales. *Quarterly Journal of the Royal Meteorological Society*, 146(729), 1822–1841. <https://doi.org/10.1002/qj.3768>
- Penland, C. (1989). Random forcing and forecasting using principal oscillation pattern analysis. *Monthly Weather Review*, 117(10), 2165–2185. [https://doi.org/10.1175/1520-0493\(1989\)117<2165:rfafup>2.0.co;2](https://doi.org/10.1175/1520-0493(1989)117<2165:rfafup>2.0.co;2)
- Ring, M. J., & Plumb, R. A. (2008). The response of a simplified GCM to axisymmetric forcings: Applicability of the fluctuation-dissipation theorem. *Journal of the Atmospheric Sciences*, 65(12), 3880–3898. <https://doi.org/10.1075/2008JAS2773.1>
- Robinson, W. A. (2000). A baroclinic mechanism for the eddy feedback on the zonal index. *Journal of the Atmospheric Sciences*, 57(3), 415–422. [https://doi.org/10.1175/1520-0469\(2000\)057<0415:abmft>2.0.co;2](https://doi.org/10.1175/1520-0469(2000)057<0415:abmft>2.0.co;2)
- Schmid, P. J., & Sesterhenn, J. (2008). *Dynamic mode decomposition of numerical and experimental data*. In *61st Annual Meeting of the APS Division of Fluid Dynamics*. American Physical Society.
- Schneider, T. (2005). Zonal momentum balance, potential vorticity dynamics, and mass fluxes on near-surface isentropes. *Journal of the Atmospheric Sciences*, 62(6), 1884–1900. <https://doi.org/10.1175/jas3341.1>
- Schneider, T., & Griffies, S. (1999). A conceptual framework for predictability studies. *Journal of Climate*, 12(10), 3133–3155. [https://doi.org/10.1175/1520-0442\(1999\)012<3133:acffps>2.0.co;2](https://doi.org/10.1175/1520-0442(1999)012<3133:acffps>2.0.co;2)
- Sheshadri, A., & Plumb, R. A. (2017). Propagating annular modes: Empirical orthogonal functions, principal oscillation patterns, and time scales. *Journal of the Atmospheric Sciences*, 74(5), 1345–1361. <https://doi.org/10.1175/JAS-D-16-0291.1>
- Simpson, I. R., Shepherd, T. G., Hitchcock, P., & Scinocca, J. F. (2013). Southern Annular Mode dynamics in observations and models. Part II: Eddy feedbacks. *Journal of Climate*, 26(14), 5220–5241. <https://doi.org/10.1175/jcli-d-12-00495.1>
- Smith, S., Lu, J., & Staten, P. W. (2024). Diabatic eddy forcing increases persistence and opposes propagation of the Southern Annular Mode in MERRA2. *Journal of the Atmospheric Sciences*, 81(4), 743–764. <https://doi.org/10.1175/JAS-D-23-0019.1>
- Son, S.-K., & Lee, S. (2007). Preferred modes of variability and their relationship with climate change. *Journal of Climate*, 19(10), 2063–2075. <https://doi.org/10.1175/jcli3705.1>
- Sparrow, S., Blackburn, M., & Haigh, J. D. (2009). Annular variability and eddy–zonal flow interactions in a simplified atmospheric GCM. Part I: Characterization of high- and low-frequency behavior. *Journal of the Atmospheric Sciences*, 66(10), 3075–3094. <https://doi.org/10.1175/2009jas2953.1>
- Stevens, B., Bony, S., & Webb, M. (2012). Clouds on-off climate intercomparison experiment (cookie). Tech. rep.
- Thompson, D. W. J., & Wallace, J. M. (2000). Annular modes in the extratropical circulation. Part I: Month-to-month variability. *Journal of Climate*, 13(5), 1000–1016. [https://doi.org/10.1175/1520-0442\(2000\)013<1000:amitec>2.0.co;2](https://doi.org/10.1175/1520-0442(2000)013<1000:amitec>2.0.co;2)
- Tippett, M. K., & Chang, P. (2003). Some theoretical consideration on predictability of linear stochastic dynamics. *Tellus A: Dynamic Meteorology and Oceanography*, 55(2), 148–157. <https://doi.org/10.3402/tellusa.v55i2.12086>
- Vallis, G. K. (2007). *Atmospheric and oceanic fluid dynamics* (1st ed., p. 745). Cambridge University Press.
- Voigt, A., Albern, N., Ceppi, P., Grise, K., Li, Y., & Medeiros, B. (2020). Clouds, radiation, and atmospheric circulation in the present-day climate and under climate change. *WIREs Climate Change*, 12(2), e694. <https://doi.org/10.1002/wcc.694>
- Voigt, A., & Shaw, T. A. (2016). Impact of regional atmospheric cloud-radiative changes on shifts of the extratropical jet stream in response to global warming. *Journal of Climate*, 29(23), 8399–8421. <https://doi.org/10.1175/JCLI-D-16-0140.1>
- Von Storch, H., Burns, T., Fischer-Burns, I., & Hasselmann, K. (1988). Principal oscillation pattern analysis of the 30- to 60-day oscillation in general circulation model equatorial troposphere. *Journal of Geophysical Research*, 93(D9), 11022–11036. <https://doi.org/10.1029/JD093iD09p11022>
- Wall, C. J., Lutsko, N. J., & Vishny, D. N. (2022). Revisiting cloud radiative heating and the Southern Annular Mode. *Geophysical Research Letters*, 49(19), e2022GL100463. <https://doi.org/10.1029/2022GL100463>
- Wang, M., Zhang, Y., & Lu, J. (2021). The evolution dynamical processes of Ural blocking through the lens of local finite-amplitude wave activity budget analysis. *Geophysical Research Letters*, 48(10), e2020GL091727. <https://doi.org/10.1029/2020GL091727>
- Woollings, T., Papritz, L., Mbengue, C., & Spengler, T. (2016). Diabatic heating and jet stream shifts: A case study of the 2010 negative North Atlantic Oscillation winter. *Geophysical Research Letters*, 43(18), 9994–10002. <https://doi.org/10.1002/2016gl070146>
- Xia, X., & Chang, E. K. (2014). Diabatic damping of zonal index variations. *Journal of the Atmospheric Sciences*, 71(8), 3090–3105. <https://doi.org/10.1175/JAS-D-13-0292.1>
- Zurita-Gotor, P., Blanco-Fuentes, J., & Gerber, E. P. (2014). The impact of baroclinic eddy feedback on the persistence of jet variability in the two-layer model. *Journal of the Atmospheric Sciences*, 71(1), 410–429. <https://doi.org/10.1175/jas-d-13-0102.1>